SOLAR AXION PRODUCTION AND DETECTION MECHANISMS

by

Umut Deniz Özuğurel

B.S., Microelectronics Engineering, Sabancı University, 2006

Submitted to the Institute for Graduate Studies in
Science and Engineering in partial fulfillment of
the requirements for the degree of
Master of Science

Graduate Program in Physics

Boğaziçi University

2009

ACKNOWLEDGEMENTS

I am grateful to Prof. Metin Arık for his guidance not only in my thesis work but also in several aspects of life. I thank Assoc. Prof. Serkant Çetin for his help, kindness and understanding. I am also thankful to Prof. Nihal Ercan for her sincere interest in my education and Assoc. Prof. Aşkın Ankay for friendly discussions. I am debtful to the CAST team that generously helped me during my stay at CERN. I would not be able to finish this thesis without the support and the trust of Ayça Beygo and my family.

ABSTRACT

SOLAR AXION PRODUCTION AND DETECTION MECHANISMS

Production mechanisms of the axion particle in the Sun as well as the detection principle and the data analysis methods that the CAST experiment is based on are reviewed. It is shown that the solar axion production can be explained both by the Primakoff effect with a reduced decay width due to plasma screening effects and by the electromagnetic plasma excitations up to a momentum limit. The analysis of CAST data which results in an upper limit on the axion-photon coupling constant for a range of axion mass is explained in connection with the solar axion flux and the detection principle. Additionally, technical details about CAST is given. Finally, a survey on data collected during the first part of the second phase of CAST is presented.

ÖZET

AKSİYON PARÇACIĞI ÜRETİM VE TESPİT MEKANİZMALARI

Aksiyon parçacığının Güneş'te üretim mekanizmalarının yanı sıra CAST deneyinin dayandığı aksiyon tespit ilkesi ve veri analiz yöntemleri gözden geçirilmiştir. Güneş aksiyonlarının üretiminin belli bir momentum değerine kadar, hem bozunma genliği plazma perdeleme etkileri yüzünden azalmış Primakoff etkisiyle, hem de elektromanyetik plazma salınımlarıyla açıklanabileceği gösterilmiştir. Aksiyon-foton etkileşim sabitine belli bir aksiyon kütle aralığı için bir üst sınır koyan, CAST verilerinin analizi Güneş aksiyonlarının akısı ve aksiyon tespit ilkesiyle bağlantılı olarak açıklanmıştır. Bunlara ek olarak, CAST ile ilgili teknik ayrıntılar verilmiştir. Son olarak, CAST deneyinin ikinci fazının ilk kısmında toplanan verilere genel bir bakış sunulmuştur.

TABLE OF CONTENTS

LIST OF FIGURES

LIST OF SYMBOLS/ABBREVIATIONS

a	Axion field
A	Detector area
$\mathbf{B}$	Magnetic field
$\mathbf{D}$	Electric displacement field
$D_\oplus$	Average solar distance from the Earth
e	Elementary charge
E	Photon energy
E_a	Axion energy
$\mathbf{E}$	Electric field
f	Scattering amplitude
f_a	Axion decay constant
f_B	Bose-Einstein distribution of thermal photon bath in the solar plasma
f_π	Pion decay constant
$F_{\mathtt{eff}}$	Effective form factor
$F_{\mu\nu}$	Electromagnetic field-strength tensor
$\tilde{F}^{\mu\nu}$	Dual electromagnetic field strength tensor
g	Axion-photon coupling constant
i	Imaginary unit
k	Photon wavenumber
$\mathbf{k}$	Photon wavevector
$\mathbf{k}_a$	Axion field wavevector
$\mathbf{k}_\gamma$	Electromagnetic field wavevector
L	Likelihood function
L_a	Axion luminosity
$\mathcal{L}_{a\gamma}$	Lagrangian of axion-photon interaction
m_a	Axion mass
m_d	Down quark mass
m_e	Electron mass

m_i	Ion mass
m_u	Up quark mass
m_π	Pion mass
n_e	Electron density
n_i	Density of plasma component of kind i
$P_{a\to\gamma}$	Probability of axion to photon conversion
$P_{\gamma\to a}$	Probability of photon to axion conversion
q	Zero degree momentum difference between axion and photon
$\mathbf{q}$	Three-momentum difference between axion and photon
r	Dimensionless radial coordinate
$R_\odot$	Solar radius
T	Temperature
T_e	Electron temperature
T_i	Temperature of plasma component of kind i
T_p	Proton temperature
$\mathbf{v}$	Fluid velocity vector
Z	Atomic number
Z_i	Atomic number of the plasma component of kind i
α	Fine structure constant
Γ	Decay rate
$\Gamma_{\gamma\to a}$	Photon to axion decay rate
δ_{ij}	Kronecker delta
$\boldsymbol{\epsilon}$	Polarization vector
ϵ_0	Permittivity constant
ϵ_l	Longitudinal dielectric permittivity
ϵ_t	Transverse dielectric permittivity
θ	Scattering angle
κ	Debye-Hückel wavenumber
κ_e	Debye-Hückel wavenumber for electrons only
κ_i	Debye-Hückel wavenumber for the plasma component of kind i

μ_i	Expected count in bin i
ρ	Charge density
σ_i	Variance
σ_p	Total cross section
Φ_a	Total axion number flux
ω	Photon frequency
ω_a	Axion frequency
ω_i	Ion plasma frequency
ω_p	Plasma frequency
ω_{pe}	Electron plasma frequency
ω_{pp}	Proton plasma frequency
$\tilde{\omega}$	Axion energy shift
Ω	Solid angle
$\Box$	D'Alembertian
∇	Gradient

CAST	CERN Axion Solar Telescope
CCD	Charge coupled device
CERN	European Organization for Nuclear Research
CP	Charge parity
LEP	Large Electron-Positron Collider
LHC	Large Hadron Collider
MicroMEGAS	Micromesh gaseous structure
MPI	Max-Planck Institute
NASA	National Aeronautics and Space Administration
TPC	Time projection chamber

1. INTRODUCTION

The quantum chromodynamics (QCD) predicts that the charge-parity (CP) symmetry is broken in strong interactions. But, the fact that the dipole moment of neutron predicted by this theory could not be observed implies that the CP symmetry is conserved in strong interactions. This problem, called the strong CP problem, is solved by the introduction of a global chiral U(1) symmetry into QCD [1]. The spontaneous breaking of this symmetry results in a pseudoscalar Nambu-Goldstone boson named the *axion* [2, 3].

Stellar plasmas are powerful sources of the axion particle. The Sun is the best place to look for axions since it is the closest star to us. In the nonrelativistic limit, which is applicable to the solar plasma, axion production in the Sun may be described by two approches. In one approach, axions are produced by the interaction of blackbody photons with electromagnetic fields of a plasma via the Primakoff effect. In the other approach, axions, treated as classical waves, are produced by the interaction of blackbody electromagnetic waves with electromagnetic fields created by charged particles of plasma. These processes are equivalent when the momentum transfer between the axion and the photon is smaller than the Debye-Hückel wavelength. If the momentum transfer is bigger than that value, the only interpretation is the Primakoff effect, whose decay width is reduced by the Debye-Hückel screening [4, 5].

The detection of solar axions is possible by the experimental method proposed by Sikivie [6]. The method relies on the fact that axions will reconvert into an X-ray photons in a high magnetic field via the the inverse-Primakoff effect. The CERN Axion Solar Telescope (CAST) is an helioscope based on this principle [7, 8]. It mainly consists of a decommisioned LHC superconducting magnet which operates with a current of 13000 A at a temperature of 1.8 K. Presently, two types of detectors are attached at the four ends of two beam pipes of the magnet, one charge coupled device (CCD) and three micromesh gaseous structures (MicroMEGAS). Before 2007 a TPC used to be attached at one end of the magnet, covering the ends of both beam pipes. It is expected

that axions will manifest themselves as excess photons over background photons.

The experiment consists of two phases. Phase I was operated for 2 years with the beam pipes evacuated. This setting was sensitive to axions with masses smaller than 0.02 eV. In this phase, a coupling limit of 8.8×10^{-11} was obtained for axion masses of $m_a \lesssim 0.02$ eV.

Phase II was divived into two parts in itself. The first part was when the pipes were filled with ^{4}He, whose pressure was changed every day to tune the sensitivity of the experiment to different axion mass values. In 160 pressure setting, a range of 0.02-0.4 eV was scanned and a limit of 2.7×10^{-10} was obtained on the axion-photon coupling constant. The second part is in progress and it uses ^{3}He as a buffer gas to scan higher axion masses, between the range 0.4-1.2 eV. The magnet points at the Sun during sunrise and sunset for 1.5 hours in each tracking. Background photons are collected during the rest of the day.

During the experiment, several condidate events were observed. Although those cases were considered as false alarms, debates are going in the collaboration about their significance and whether there are possible axion sources for them. As a first step towards solving these topics, the events collected during Phase II with ^{4}He were gathered together and presented as plots.

2. THE AXION PARTICLE

2.1. Production

2.1.1. Primakoff Effect

The axion particle may be created by the interaction of a photon with an electromagnetic field due to its two photon vertex [9, 4]. This process is called the *Primakoff effect*, proposed by Primakoff to explain the decay of a neutral pion into a photon in an electromagnetic field [10]. Since the axion is a pseudoscalar particle like pion, this effect is conveniently adapted to the axion production. In the nonrelativistic solar plasma, where $T/m_e \ll 1$, the Primakoff effect is the dominant process of axion production [11].

The coupling of an axion to two photons is described by the Lagrangian density[1]

$$\mathcal{L}_{a\gamma} = -\frac{1}{4} g F_{\mu\nu} \tilde{F}^{\mu\nu} a = g \mathbf{E} \cdot \mathbf{B}\, a, \tag{2.1}$$

where g is a coupling constant of dimension (energy)$^{-1}$, a the pseudoscalar axion field, F the electromagnetic field strength tensor and $\tilde{F}$ is its dual, $\mathbf{E}$ the electric field and $\mathbf{B}$ the magnetic field. $\mathcal{L}_{a\gamma}$ is invariant under CP transformation because $\mathbf{E} \cdot \mathbf{B}$ is a pseudoscalar due to the fact that $\mathbf{E}$ is a vector and $\mathbf{B}$ is a pseudovector. The coupling constant is given by

$$g = \frac{\alpha}{2\pi} \frac{1}{f_a} \left(\frac{E}{N} - \frac{2}{3} \frac{4+z}{1+z} \right), \tag{2.2}$$

where $z \equiv m_u/m_d$, mass ratio of up and down quarks, f_a is the axion decay constant and E and N are the electromagnetic and the color anomalies.

[1] Heaviside-Lorentz units with $c = \hbar = k_B = 0$ are used in this thesis.

The mass of the axion is given by

$$m_a = \frac{z^{1/2}}{1+z}\frac{f_\pi m_\pi}{f_a}, \tag{2.3}$$

where m_π is the pion mass and f_π is the pion decay constant. Therefore, the $g - m_a$ relation is given by

$$g = \frac{\alpha}{2\pi}\left(\frac{E}{N} - \frac{2}{3}\frac{4+z}{1+z}\right)\frac{1+z}{z^{1/2}}\frac{m_a}{m_\pi f_\pi}, \tag{2.4}$$

where m_a is the axion mass, α is the fine structure constant. This equation describes a band in the $g - m_a$ plane where the axion would exist since E/N is model dependent and z is uncertain [12]. The decay width of an axion into two photons is found [4]

$$\Gamma = \frac{g^2}{64}\frac{m_a^3}{\pi}. \tag{2.5}$$

If a photon with energy ω is incident on a localized distribution of charge $\rho(\mathbf{r})$ in a medium, the cross section of the Primakoff effect is [4]

$$\frac{d\sigma_p}{d\omega} = \frac{1}{2}\left(\frac{e}{4\pi}\right)^2 g^2 \frac{(\mathbf{k}_\gamma \times \mathbf{k}_a)^2}{\mathbf{q}^4}|F(\mathbf{q})|^2, \tag{2.6}$$

where $\mathbf{q} = \mathbf{k}_\gamma - \mathbf{k}_a$ is the three-momentum difference between the axion and the photon and $F(\mathbf{q})$ is the form factor of the charge distribution, which is

$$F(\mathbf{q}) = \frac{1}{e}\int d^3\mathbf{r}\rho(\mathbf{r})e^{i\mathbf{q}\cdot\mathbf{r}}. \tag{2.7}$$

We know that the dominant contribution to the Primakoff effect is from forward scattering [13]. This means that the momentum vector of the axion is mostly parallel to that of the photon. Therefore the zero degree momentum transfer between the axion

and the photon is

$$q = \sqrt{\omega^2 - m_a^2} - \sqrt{\omega^2 - \omega_p^2}, \tag{2.8}$$

where ω is the energy of the photon and ω_p is the plasma frequency which behaves as the effective mass of the photon (appendix). Therefore, assuming that the plasma frequency of the medium ω_p and the axion mass m_a are smaller than the energy of the photon ω, the differential cross section is to lowest order [4]

$$\frac{d\sigma_p}{d\omega} = \frac{1}{2}\left(\frac{e}{4\pi}\right)^2 g^2 \frac{\sin^2\theta}{[2(1-\cos\theta) + (q/\omega)^2\cos\theta]^2}|F(\mathbf{q})|^2, \tag{2.9}$$

where θ is the scattering angle and

$$q = \frac{m_a^2 - \omega_p^2}{2\omega} \tag{2.10}$$

in the aforementioned limit.

If the target is a pointlike charge of magnitude Ze, then the form factor is $|F|^2 = Z^2$, independent of the momentum transfer. Then, at small scattering amplitudes

$$\frac{d\sigma_p}{d\omega} = \frac{1}{2}\left(\frac{e}{4\pi}\right)^2 g^2 Z^2 \frac{\theta^2}{[\theta^2 + \ (q/\omega)^2]^2} \tag{2.11}$$

Finally, the total cross section is [4]

$$\sigma_p = \frac{Z^2 g^2}{4}\frac{e^2}{4\pi}\left[\ln\left(\frac{2\omega}{q}\right) - 1\right]. \tag{2.12}$$

Noticing $\alpha = e^2/4\pi$ and plugging in $q = m_a^2/2\omega$, we get

$$\sigma_p = Z^2 g^2 \alpha\left[\frac{1}{2}\ln\left(\frac{2\omega}{m_a}\right) - \frac{1}{4}\right]. \tag{2.13}$$

But, this total cross section is valid in vacuum where an isolated point charge is taken into account or in a very dilute or a very hot plasma where the electromagnetic interactions between charges may be neglected. When the medium is a real plasma, every charge creates a cloud of charges around itself by attracting charges of the opposite sign and repelling charges of the same sign [14]. Therefore, the electric field around a charge is modified by this nontrivial distribution of charges. This fact requires a redefinition of the form factor.

Taking into account the correlation of the positions of charges, which is homogeneous for particles apart from each other by a distance called the *Debye-Hückel radius* (Appendix A), we get a new effective form factor for every individual particle as [4]

$$|F_{\mathtt{eff}}(\mathbf{q})|^2 = Z^2 \frac{|\mathbf{q}|^2}{\kappa^2 + |\mathbf{q}|^2} \tag{2.14}$$

where κ^2 is the square of the inverse Debye-Hückel radius and defined by (see Appendix A)

$$\kappa^2 = \frac{e^2}{T} \sum_{i=1}^{N} Z_i^2 n_i, \tag{2.15}$$

where Z_i is the atomic number, which is -1 for electron, and n_i is the number density. This equation means that the Debye-Hückel radius of a plasma depends on the number density of its components which are electrons and nuclei of different atomic number.

With $F_{\mathtt{eff}}(\mathbf{q})$, the differential cross section of the Primakoff effect in a plasma becomes [4]

$$\frac{d\sigma_p}{d\Omega} = \frac{Z^2 g^2}{8} \left(\frac{e}{4\pi}\right)^2 \frac{1+\cos(\theta)}{1+2(\kappa/2\omega)^2 - \cos(\omega)} \tag{2.16}$$

Integrating over the scattering angles, we get the total cross section as [4]

$$\sigma_p(\omega) = \frac{e^2}{32\pi} g^2 Z^2 \left[\left(1 + \frac{\kappa^2}{4\omega^2}\right) \ln\left(1 + \frac{4\omega^2}{\kappa^2}\right) - 1\right] \tag{2.17}$$

Summing over all targets and assuming that the plasma is pure hydrogen so that $Z^2 = 1$, the transition rate of a photon of frequency ω into an axion of the same energy is found as [4]

$$\Gamma_{\gamma\to a} = \frac{g^2 T\kappa^2}{32\pi}\left[\left(1+\frac{\kappa^2}{4\omega^2}\right)\ln\left(1+\frac{4\omega^2}{\kappa^2}\right)-1\right]. \tag{2.18}$$

2.1.2. Electromagnetic Plasma Fluctuations

In case of a nonrelativistic and nondegenerate plasma, axion production can be formulated in classical terms. The process, in this limit, is seen as the conversion of a classical transverse electromagnetic wave into a classical axion wave in an electric field $\mathbf{E}(\mathbf{x})$ [14]. The classical equation of motion of an axion wave derived from the interaction Lagrangian (2.1) then is [6]

$$(\Box + m_a^2)a = g\mathbf{E}\cdot\mathbf{B}, \tag{2.19}$$

where $\Box = \partial_t^2 - \nabla^2$ and a is the axion wave. The two-photon interaction term $\mathbf{E}\cdot\mathbf{B}$ in equation (2.1) corresponds to the source term of equation (2.19). Thermal electromagnetic radiation of a plasma and the collective and random motions of the charged particles in that solar plasma causes the fluctuation of this source term, which results in emission of solar axions [14].

The role of the fluctuation of $\mathbf{E}\cdot\mathbf{B}$ is seen by investigating the differential transition rate of the aforementioned process. The scattering amplitude for the conversion of a classical transverse electromagnetic wave into a classical axion wave in an electric field $\mathbf{E}(\mathbf{r})$ is [5]

$$f(\Omega) = \frac{g}{4\pi}(\boldsymbol{\epsilon}\times\mathbf{k_t})\cdot\int d^3\mathbf{r}e^{-i\mathbf{q}\cdot\mathbf{r}}\mathbf{E}(\mathbf{r}), \tag{2.20}$$

where $\mathbf{q} = \mathbf{k_a} - \mathbf{k_t}$, i.e. the momentum difference between the transverse electromagnetic wave $\mathbf{k_t}$ and the axion wave $\mathbf{k_a}$. $\boldsymbol{\epsilon}$ is the polarization vector of the transverse

electromagnetic wave with $\boldsymbol{\epsilon} \cdot \mathbf{k_t} = 0$. Remember $d\Gamma/d\Omega = |f(\Omega)|^2$, then

$$\frac{d\Gamma}{d\Omega} = |f(\Omega)|^2 = \frac{g^2}{(4\pi)^2}(\boldsymbol{\epsilon} \times \mathbf{k_t})_i(\boldsymbol{\epsilon} \times \mathbf{k_t})_j \int d^3\mathbf{r} \int d^3\mathbf{r}' E_i(\mathbf{r})E_j(\mathbf{r}')e^{-i\mathbf{q}\cdot(\mathbf{r}-\mathbf{r}')}, \quad (2.21)$$

where repeated indices are summed. The integral terms in equation (2.21) are the Fourier transformations of $E_i(\mathbf{r})$ and $E_j(\mathbf{r}')$, thus we may rewrite this equation as

$$\frac{d\Gamma}{d\Omega} = \frac{g^2}{(4\pi)^2}(\boldsymbol{\epsilon} \times \mathbf{k_t})_i(\boldsymbol{\epsilon} \times \mathbf{k_t})_j \; E_i(-\mathbf{q})E_j(\mathbf{q}) \quad (2.22)$$

If $\mathbf{E}(\mathbf{r})$ randomly fluctuates, we should take the ensemble average of the Fourier components $E_i(-\mathbf{q})$ and $E_j(\mathbf{q})$ of $\mathbf{E}(\mathbf{r})$, noted by $< E_i(-\mathbf{q})E_j(\mathbf{q}) >$ [14].

$$\frac{d\Gamma}{d\Omega} = \frac{g^2}{(4\pi)^2}(\boldsymbol{\epsilon} \times \mathbf{k_t})_i(\boldsymbol{\epsilon} \times \mathbf{k_t})_j < E_iE_j >_{\mathbf{q}}, \quad (2.23)$$

where $< E_iE_j >_{\mathbf{q}} \equiv < E_i(-\mathbf{q})E_j(\mathbf{q}) >$ is the correlation function of the Fourier components of the electric field, i.e. the Fourier transform of the spatial correlation function $< E_i(\mathbf{r})E_j(\mathbf{r}') >$. When the time dependence of the electric field is included, the energy of the axions slightly shifts. The probability of this shift is determined by the spectral density of the correlation function $< E_iE_j >_{\mathbf{q}}$, noted by $< E_iE_j >_{\mathbf{q}\tilde{\omega}}$.

$$\frac{d\Gamma}{d\tilde{\omega}d\Omega} = \frac{g^2}{(4\pi)^2}(\boldsymbol{\epsilon} \times \mathbf{k_t})_i(\boldsymbol{\epsilon} \times \mathbf{k_t})_j \; \frac{< E_iE_j >_{\mathbf{q}\tilde{\omega}}}{2\pi} \quad (2.24)$$

where $\tilde{\omega}$ is the energy shift of the axion, that is $\tilde{\omega} = \omega_a - \omega_t$. Using the fluctuation-dissipation theorem, the spectral density of the correlation function of the Fourier components of the electric field becomes [15]

$$< E_iE_j >_{\mathbf{q}\tilde{\omega}} = \frac{2}{e^{\tilde{\omega}/T} - 1}\left[\frac{q_iq_j}{\mathbf{q}^2}\frac{\mathrm{Im}(\epsilon_l)}{|\epsilon_l|^2} + \left(\delta_{ij} - \frac{q_iq_j}{\mathbf{q}^2}\right)\frac{\mathrm{Im}(\epsilon_t)}{|\epsilon_t - \mathbf{q}^2/\tilde{\omega}^2|^2}\right], \quad (2.25)$$

where ϵ_l and ϵ_t are the longitudinal and transverse dielectric permittivities of the medium (see Appendix B). The term $\mathrm{Im}(\epsilon_l)/|\epsilon_l|^2$ is the spectral density of the longitudinal fluctuations and $\mathrm{Im}(\epsilon_t)/|\epsilon_t - \mathbf{q}^2/\tilde{\omega}^2|^2$ is the spectral density of the transverse

fluctuations[14]. Transverse fluctuations can always be neglected for two reasons. First, if $\omega/\omega_p \ll k/\kappa_e$, then transverse fluctuations are proportional to $\delta(\omega^2-\omega_p^2-k^2)$ and so they represent transverse transverse plasmons of dispersion relation $\omega^2-\omega_p^2-k^2$, the nonrelativistic limit of the equation (B.26). But, this part of the fluctuations spectrum does not contribute due to energy-momentum conservation. Second, if $\omega/\omega_p \lesssim k/\kappa_e$, the power in transverse fluctuations is much smaller than that in longitudinal ones [5].

Assuming the energy shift ω is small compared to T, we find the differential decay rate as

$$\frac{d\Gamma}{d\tilde{\omega}d\Omega} = \frac{g^2}{(4\pi)^2}(\boldsymbol{\epsilon}\times\mathbf{k_t})_i(\boldsymbol{\epsilon}\times\mathbf{k_t})_j \ \frac{2T}{\tilde{\omega}}\frac{1}{2\pi}\frac{q_iq_j}{\mathbf{q}^2}\frac{\mathrm{Im}(\epsilon_l)}{|\epsilon_l|^2} \tag{2.26}$$

Rearranging terms, we get

$$\frac{d\Gamma}{d\tilde{\omega}d\Omega} = \frac{g^2}{(4\pi)^2}\frac{|(\mathbf{e}\times\mathbf{k_t})\cdot\mathbf{q}|^2}{\mathbf{q}^2} \ \frac{T}{\pi\omega_p}\frac{\omega_p}{\tilde{\omega}}\frac{\mathrm{Im}(\epsilon_l)}{|\epsilon_l|^2}. \tag{2.27}$$

The $d\tilde{\omega}$ integration gives

$$< E_iE_j >_{\mathbf{q}} = \frac{q_iq_j}{\mathbf{q}^2} \ \frac{T}{1+\mathbf{q}^2/2\kappa_e^2}, \tag{2.28}$$

where $\kappa_e = \sqrt{N_e e^2/T\epsilon_0}$, the Debye-Hückel wavenumber for the electrons only. Finally, the total decay rate of a transverse electromagnetic wave into an axion wave is [5]

$$\Gamma = \frac{g^2T\kappa^2}{32\pi} \ \left[\left(1+\frac{\kappa^2}{4\omega^2}\right)\ln\left(1+\frac{4\omega^2}{\kappa^2}\right)-1\right], \tag{2.29}$$

where $\kappa^2 = 2\kappa_e^2$, κ being the total inverse screening scale in a pure hydrogen plasma.

This decay rate is identical to the one obtained in the previous section (equation (2.18)). But, this one is only applicable when the condition $\omega \lesssim \kappa_e$ is satisfied [5], because otherwise longitudinal electromagnetic waves cannot exist due to Landau damping [16].

2.2. Solar Axion Flux

The total axion number flux at Earth is [7]

$$\Phi_a = \frac{R_\odot^3}{4\pi D_\oplus^2} \int_0^1 dr\, 4\pi\, r^2 \int_{\omega_p}^\infty dE \frac{4\pi k^2}{(2\pi)^3} \frac{dk}{dE} 2 f_B \Gamma_{\gamma\to a}, \tag{2.30}$$

where $R_\odot$ is the solar radius, $D_\oplus$ is the average solar distance from the Earth, $r = R/R_\odot$ is the dimensionless solar radius variable, $\Gamma_{\gamma\to a}$ is the decay rate of a photon with energy E into an axion of the same energy, given by equation (2.18) and $f_B = (e^{E/T} - 1)^{-1}$ is the Bose-Einstein distribution of the thermal photons in the solar plasma. After simplification, we get

$$\Phi_a = \frac{R_\odot^3}{\pi^2 D_\oplus^2} \int_0^1 dr\, r^2 \int_{\omega_p}^\infty dE\, E\, k\, f_B \Gamma_{\gamma\to a}. \tag{2.31}$$

Then, the solar axion luminosity is obtained by multiplying equation (2.31) by $4\pi D_\oplus^2$ as

$$L_a = \frac{4R_\odot^3}{\pi} \int_0^1 dr\, r^2 \int_{\omega_p}^\infty dE\, E\, k\, f_B \Gamma_{\gamma\to a}. \tag{2.32}$$

Differentiating equation (2.30) with respect to the photon energy E, we get the differential axion number flux at Earth as

$$\frac{d\Phi_a}{dE} = \frac{R_\odot^3}{D_\oplus^2} \frac{1}{\pi^2} \int_0^1 dr\, r^2\, E\, k\, f_B \Gamma_{\gamma\to a}. \tag{2.33}$$

Equation (2.30) is sufficient in describing the solar axion flux if the Sun is taken as a point source. But if we want to treat the Sun as a disk, an apparent surface luminosity $\phi_a(E, r)$ (in units of cm^{-2} sec^{-1} keV^{-1} per unit surface area) of the solar disk should be introduced [17]. Therefore, the total axion number flux becomes

$$\Phi_a = 2\pi \int_0^1 dr\, r \int_{\omega_p}^\infty dE\, \phi(E, r), \tag{2.34}$$

where ω_p is the plasma frequency which depends on the radial position in the Sun since the electron density n_e of the solar plasma is variable. Comparing this equation with equation (2.31) and after some change of variables, we get [17]

$$\phi_a(E,r) = \frac{R_\odot^3}{2\pi^3 D_\oplus^2} \int_1^r ds \, \frac{s}{\sqrt{s^2 - r^2}} \, E\, k\, f_B\, \Gamma_{\gamma\to a}, \tag{2.35}$$

where s is the radial position in the Sun projected on a 2-dimensional disk.

Taking the relevant parameters from the 2004 solar model of Bahcall and Pinsonneault [18], we get the solar axion spectrum and luminosity as shown in figures 2.1 and 2.2.

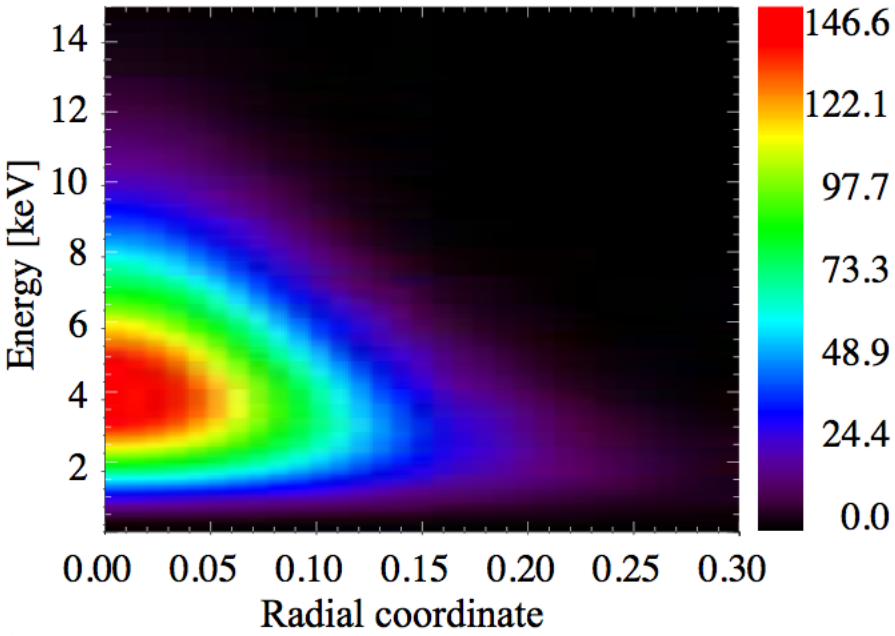

Figure 2.1. Solar axion surface luminosity on Earth, ϕ_a, as a function of radial coordiante r and axion energy E, in units of $\mathrm{cm}^{-2}\ \mathrm{sec}^{-1}\ \mathrm{keV}^{-1}$ per unit surface area on the solar disk [8]

An analytical approximation to the numerical result of the solar axion flux is

$$\frac{d\Phi_a}{dE} = 6.020 \times 10^{10}\,\mathrm{cm}^2\,\mathrm{s}^{-1}\mathrm{keV}^{-1}\, g_{10}^2\, E^{2.481} e^{-E/1.205}, \tag{2.36}$$

where E is in keV and $g_{10} = g/(10^{-10}\,\mathrm{GeV}^{-1})$ [17].

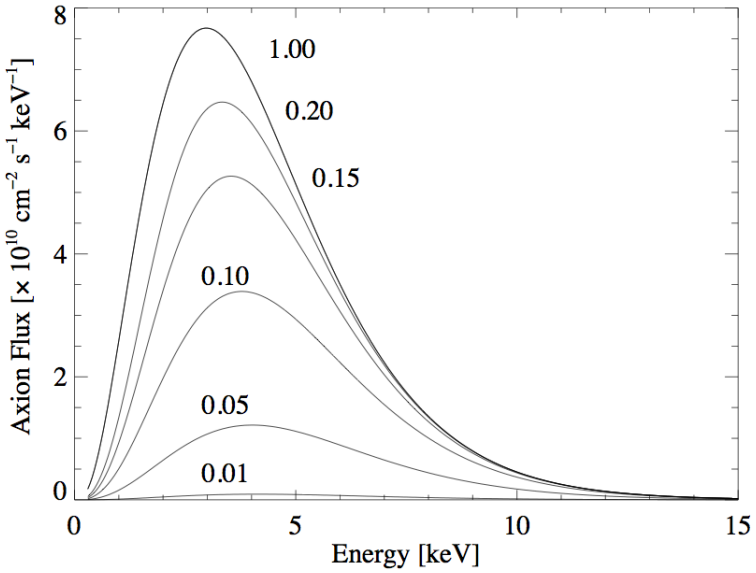

Figure 2.2. Differential solar axion flux. Each curve represents flux coming from a solar disk surface area of radius r [7].

2.3. Detection

Equation (2.1) implies that axions may be reconverted into photons in a high magnetic field. This fact can be used to detect solar axions by pointing a detector, inside of which there is a magnetic field, at the Sun [6]. The reconversion of photons into axions, i.e. the inverse Primakoff effect, is possible both in vacuum and in a buffer gas [19]. In case of vacuum, an experiment built on such principle is sensitive to a range of axion mass whereas when a buffer gas is used to adjust the sensitivity of the experiment to a very narrow mass range which can be considered as a specific mass.

The conversion probability of an axion into a photon in a transverse magnetic field B of length L in vacuum is given by [19]

$$P_{a\to\gamma} = \left(\frac{gB}{q}\right)^2 \sin^2\left(\frac{qL}{2}\right), \tag{2.37}$$

where B is the magnetic field and q is given by equation (2.10) with the plasma frequency ω_p vanished, i.e. $q = m_a^2/2E$.

In order to investigate the behavior of equation (2.37), we introduce $x = qL/2$ and get

$$P_{a\to\gamma} = \left(\frac{gBL}{2}\right)^2 \frac{\sin^2(x)}{x^2}. \tag{2.38}$$

equation (2.38) declines rapidly when $x \gtrsim 1$ (Figure 2.3). Therefore the conversion probability of an axion into a photon is favorable with such momentum transfers that [20]

$$qL \lesssim \pi. \tag{2.39}$$

This inequality is called the *coherence condition*, which quantum field theoretically implies the condition that the phase of the axion and the photon fields are coherent. In an experiment where the only unknown variable in equation (2.37) is the axion mass m_a, the coherence condition defines the axion mass sensitivity of that experiment.

The sensitivity of an experiment can be extended beyond that in case of vacuum by the introduction of a buffer gas. When a buffer gas is present over the magnetic field region where the conversion of an axion into a photon is supposed to happen, the conversion probability of an axion to a photon becomes [19]

$$P_{a\to\gamma} = \left(\frac{gB}{2}\right)^2 \frac{1}{q^2 + \Gamma^2/4}\ [1 + e^{-\Gamma L} - 2e^{-\Gamma L/2}\cos(qL)], \tag{2.40}$$

where Γ is the inverse absorption length of a photon in a buffer gas and depends on the density (and so the pressure) of that gas and q is given by equation (2.10). Note that equation (2.37) is recovered when $\Gamma \to 0$. The coherence condition is again

$$qL \lesssim \pi. \tag{2.41}$$

The coherence condition implies a sensitivity of axion masses in the range

$$\sqrt{\omega_p^2 - \frac{2\pi E}{L}} \leq m_a \leq \sqrt{\omega_p^2 + \frac{2\pi E}{L}}. \tag{2.42}$$

If E/L is very small compared to ω_p^2, the coherence is obtained at a very narrow mass range (Figure 2.3). The sensitivity for an axion mass of interest can be obtained by adjusting the electron density n_e of the medium. If the medium is kept at a constant temperature and volume, the electron density can ben adjusted by changing the pressure of the medium.

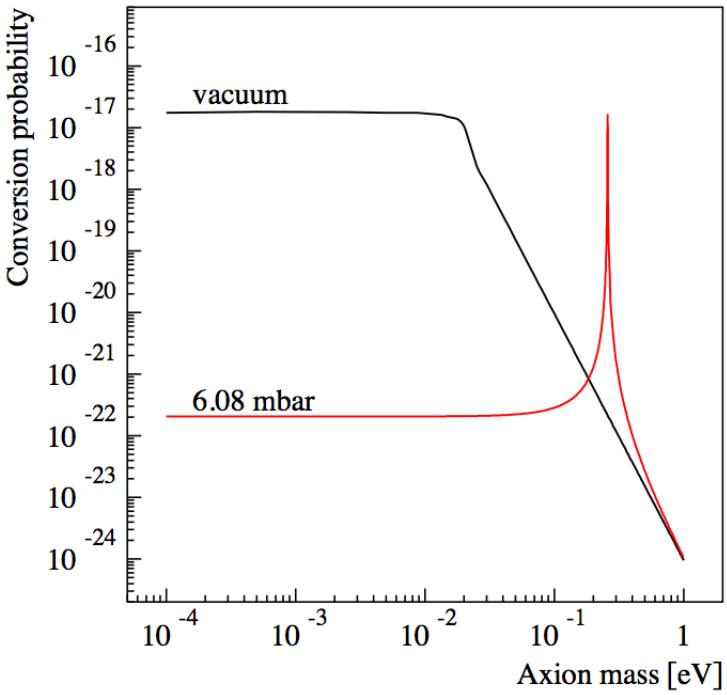

Figure 2.3. Conversion probability in case of vacuum (black curve) and with a buffer gas (red curve). Values are taken from the CAST experiment, assuming $g = 10^{-10}\,\mathrm{GeV}^{-1}$ [8].

3. THE CAST EXPERIMENT

The CAST experiment is a solar helioscope experiment based on the experimental method proposed by Sikivie [6]. Basically, it consists of a prototype superconducting LHC magnet, three types of X-ray detectors, a cryogenics system and a tracking system. It tracks the Sun during its rise and its set for about 3 hours to detect solar axions. While passing through the strong magnetic field in the beam pipes of the LHC magnet, axions are expected to be converted to photons which will be detected by detectors connected to the ends of the magnet. As mentioned earlier, axions can transform to X-ray photons in vacuum as well as in a buffer gas. CAST was operated with evacuated beam pipes in 2003 and 2004. Due to the coherence condition, during the vacuum phase (Phase I) the sensitivity for the axion mass was limited to 0.02 eV. This phase with no axions observed resulted in an axion to photon coupling upper limit of 8.8×10^{-11} GeV^{-1} with a confidence level of 95% [7].

In order to attain sensitivity for higher axion masses, beam pipes of the magnet were filled with a buffer gas in Phase II of the experiment so that reconverted photons gain an effective mass while going through beam pipes. Phase II consists of two parts differing by the buffer gas used. During the first part of Phase II in 2005 and 2006, the CAST experiment was performed with beam pipes filled with ^{4}He as a buffer gas. At each tracking run, the pressure of the gas was changed to adjust the sensitivity of the experiment for a specific axion mass. With 160 different pressure steps of about 0.8 mbar, a pressure range of 0.08-13.43 mbar, corresponding to an axion mass range from 0.02 eV to 0.4 eV, was scanned. Since no excess photons over the background photons collected in nontracking conditions were observed during this period, the danalysis of data set an upper limit on the axion-photon coupling constant of $g \lesssim 2.17 \times 10^{-10}$ GeV^{-1} [8]. For the second part of the Phase II, ^{3}He is used as a buffer gas to scan even higher axion masses from 0.4 eV to 1.2 eV. This phase is in progress and will be

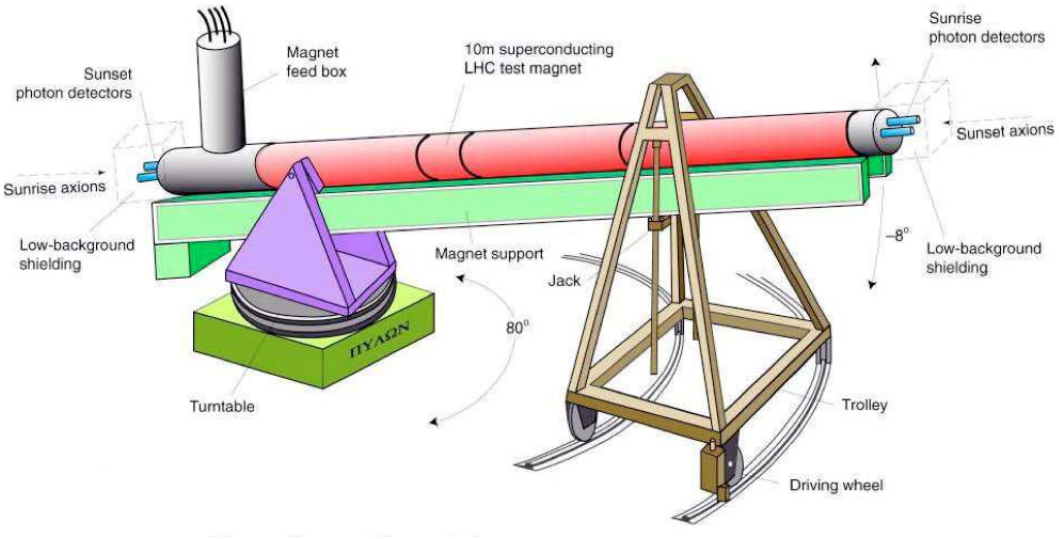

Figure 3.1. Schematic of the CAST experiment [21]

completed in 2010.

3.1. Magnet

CAST uses a decommissioned prototype LHC superconducting magnet. The magnet becomes superconducting at a temperature of about 4.5 K and creates a magnetic field of 9 T when operated at 13 kA, which is the maximum current sustainable by the magnet. A 9.26 m long uniform magnetic field transverse to the horizontal axis of the magnet, thus to the direction of axion propagation, is created inside two straight beam pipes of the magnet. There are two beams pipes, called *cold bore*, because the magnet is designed to direct proton beams in opposite directions. These cold bores, of 42.5 mm aperture, is where the inverse Primakoff conversion is supposed to take place [22].

Although 4.5 K is enough to make the magnet superconducting, the magnet is operated at a temperature of 1.8 K so that the liquid helium (^{4}He) used for cooling is superfluid. A cryogenics system installed by refurbishing instruments from the former LEP experiments is used for cooling [23]. The superfluidity of the helium has some roles. It prevents temperature gradients of the superconducting material of the magnet due to its infinite thermal conductivity. It also maintains the homogeneity of the temperature

of the liquid helium so that the magnet can be operated on a variable slope, i.e. the magnet can track the Sun without any helium convection. Finally, it ensures that the helium vessel is filled completely thanks to its zero viscosity.

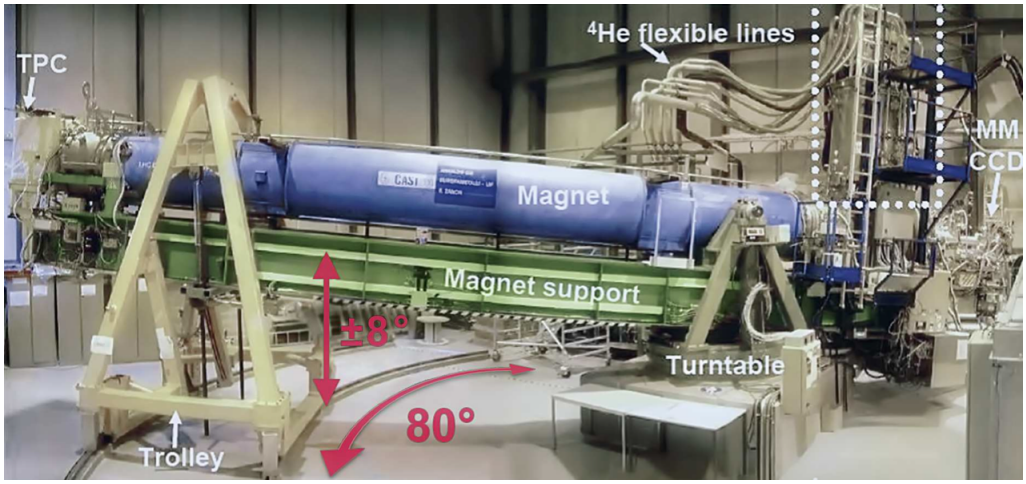

Figure 3.2. The CAST experiment [24]

3.2. Tracking

CAST is able to track the Sun with an allowed vertical and horizontal motion of ±8° and ±40° respectively, with an accuracy of better than 0.01°. It is mounted on a pivot which supports an controls the motions. The motion of the magnet is controlled by a tracking software which also records important parameters to be used in data analysis and in investigations in case of problems. [25]

3.3. Detectors

The fact that a few photons are expected during a 3 hours tracking requires the use of detectors with very low background. A charge coupled device (CCD), a time projection chamber (TPC) and a micromesh gaseous structure (MicroMEGAS) was used during Phase I and Phase II with ^{4}He. Before the start of Phase II with ^{3}He, TPC was replaced by two micromegas due to their lower level of background noise.

The detectors covers cold bores of the magnet. TPC used to be at one side of

the magnet, covering both bores, aiming to detect photons reconverted from axions coming from the Sun during its set, simply called *sunset axions*. Each of the two new MicroMEGAS which replaces it now covers same bores in a seperate manner. The other detectors are attached to the other side of the magnet, seperately covering the other ends of the bores. In addition, there is an X-ray mirror telescope between the magnet and the CCD that focuses incoming X-rays onto the CCD, dramatically reducing its background noise.

3.3.1. Time Projection Chamber

TPC is a conventional three dimensional gas detector with high gain, good efficiency and low threshold at the keV level. It has also position sensitivity to distinguish X-ray photons coming from the cold bores (Figure 3.3). It has a conversion volume of dimensions 10 cm×15 cm×30 cm filled with gas which is a mixture of 95% argon and 5% methane. X-ray photons propagate through the conversion volume and produce ionization electrons (Figure 3.4).

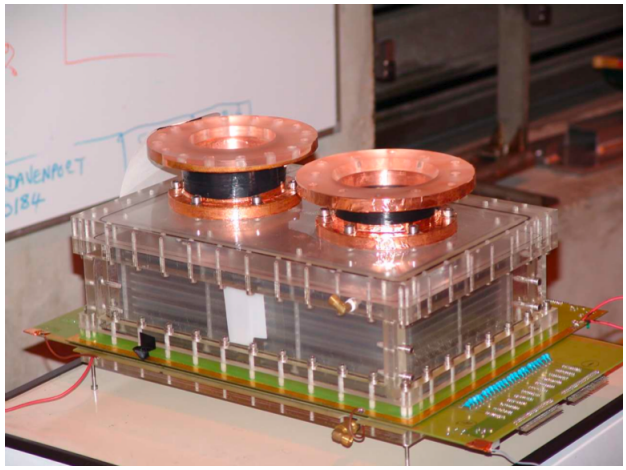

Figure 3.3. The TPC detector [27]

Total conversion takes place for photons of energy up to 6 keV propagating in the maximum drift distance of 10 cm in the direction parallel to the cold bores. The conversion effieciency decreases with energy higher than 6 keV, reaching a value of 50 %. Then, these electrons are drifted by the strong electric field of magnitude 700 V/cm towards the anode and cathode layers, where readout takes place. The anode layer is composed of 48 wires of 20 μm diameter and the cathode layer of 96 wires of 100 μm

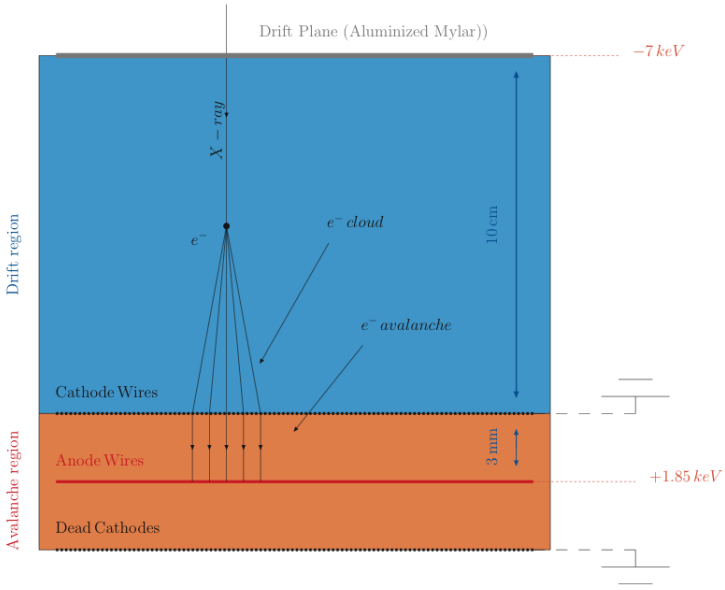

Figure 3.4. The working principle of the TPC detector [24]

diameter [26].

3.3.2. Charge Coupled Device

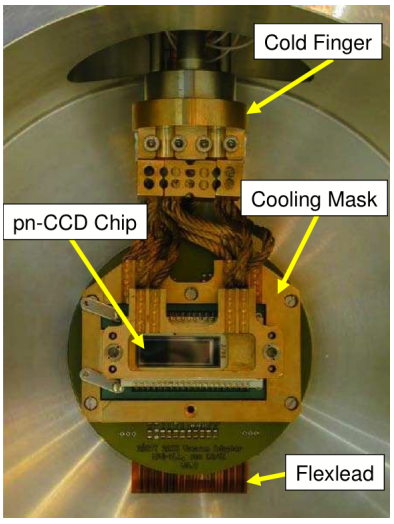

Figure 3.5. The CCD detector [29]

CCD is a semiconductor detector with high detection efficiency, low noise level and very fast read-out time. The one which is used in CAST is a prototype developed by the Max-Planck Institute Semiconductor Laboratory for X-ray astronomy. It has a sensitive area of 288 mm^2 and is composed of 200 horizontal and 64 vertical pixels,

each of which of size of $150 \times 150 \mu m^2$.

The X-ray telescope is also a prototype developed by the same institution. It focuses X-rays into an area of 6 mm^2 on the CCD, therefore dramatically increasing the signal to noise ratio. Other methods to reduce background noise are passive shielding using copper and lead to prevent noise from reaching the detector and the use of pattern recognition algorithms to reject unwanted signals read by the detector. Since the detector operates continously, it does not have any dead time [28].

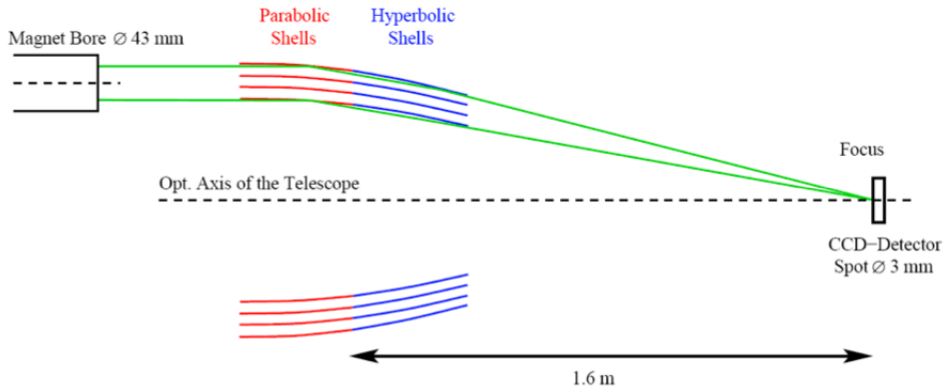

Figure 3.6. The X-ray telescope of the CCD detector [30]

3.3.3. Micromesh Gaseous Structure

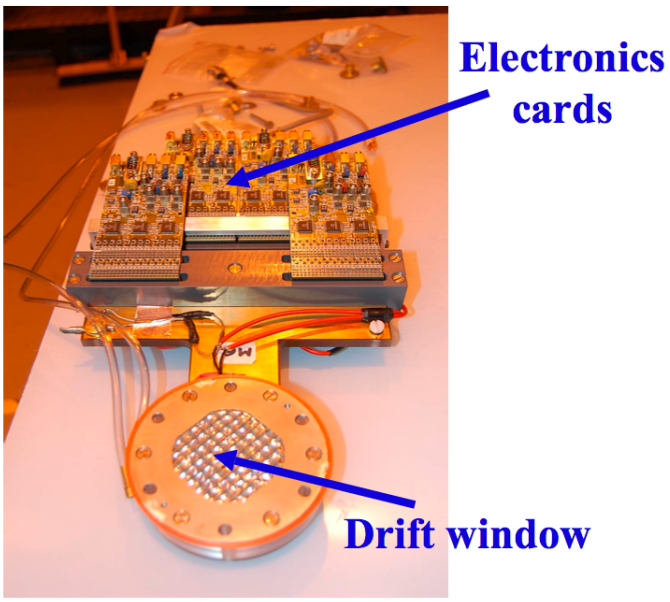

Figure 3.7. The MicroMEGAS detector [32]

MicroMEGAS is the other gaseous detector of CAST (Figure 3.7). It has a very

low background noise due to the use of low natural radioactivity materials. Its charge collection plane consists of 192 X and 192 Y strips of 350 μm pitch (Figure 3.8).

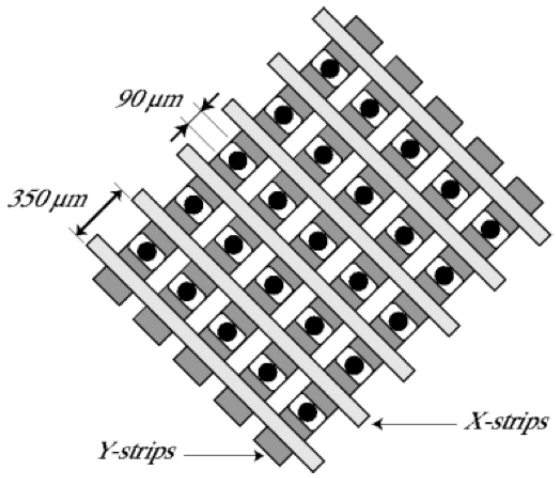

Figure 3.8. The X-Y strips of the MicroMEGAS detector [31]

It has two regions filled with gas which is a mixture of 95 % argon and 5 % isobutane. The first region is the conversion region which is 3 cm thick. An incoming X-ray photon creates a photoelectron in this region. Then, the photoelectron is drifted in the electric field (250 v/cm) of this region and creates ionization electrons until it reaches the micromesh, which seperates the amplification region from the conversion region. The electrons continue to the 0.1 mm thick amplification region while creating a pulse on the micromesh. In the amplification region, ionization electrons create an avalanche due to the very high electric field of 40kV/cm (Figure 3.9). Finally, this electron avalanche is detected by the X-Y strip of the anode plane [31].

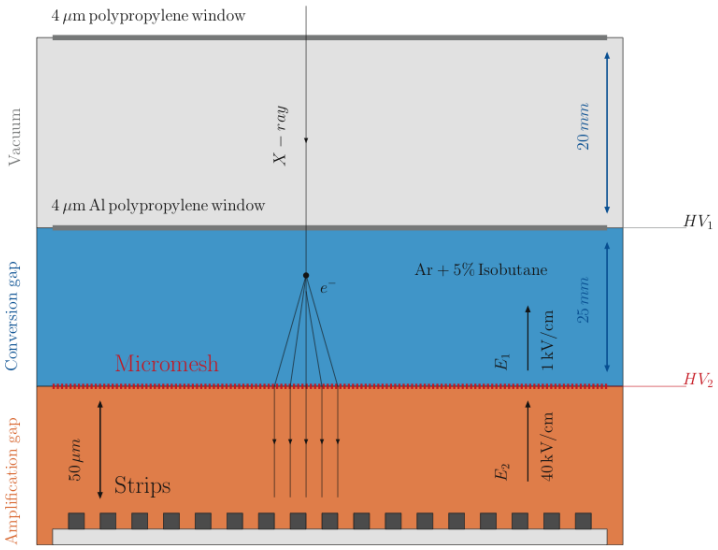

Figure 3.9. The working principle of the MicroMEGAS detector [24]

4. DATA TREATMENT

4.1. Data Acquisition

Three types of data are collected: dark or pedestal run, calibration run and tracking run. Dark run is to measure the noise of the detector when there is no data acquisition. Calibration run is done to calibrate the gain of a detector, that is to force it give the known spectrum of a radioactive source, ^{55}Fe. Tracking run is done during the rest of the day although its name implies that it is done only during the tracking. It is during this run that experimental data are acquired. Then, these data are analyzed by some routines, i.e. *quick-look analysis* is performed each day, to have quick results about events counts. If the event count of a trackingis a few σ's higher than the expected value obtained by averaging background count of the last three day, a Monte Carlo protocole is run to discover whether this excess count is suspicious or not. Each detector has different data acquisition routines and quick-look analysis routines.

4.1.1. CCD

Data acquisition starts 10 minutes before tracking starts. During that time interval, dark run and calibration run are done. Raw data are automatically transfered to the archives of TUD, Freiburg and MPI and using HEASOFT, converted to FITS, a format developed by NASA widely used in astronomy. In this format, parameters of data are stored under different keywords. Using some routines, relevant events are extracted and stored as FITS files again. Analysis of the selected data to obtain a limit on the axion-photon coupling is done using C++ with ROOT headers after they are transformed into ASCII files [21].

4.1.2. TPC

Data acquired in each run are stored in CASTOR. There is no distinction between tracking and background run; data are recorded continuously. A program written in C

using ROOT classes analyzes data to extract useful event information. First, location of an event is determined. Then, clusters are built. Since a wave hits the detector, several neighbor wires are hit. But, since X-ray events are of interest, hits whose time difference are less than 0.05 μm are taken as clusters. Finally, some cuts based on calibration tests done in the Panter facility at MPI are applied to data and leaves events of interest only. These events are stored in ROOT files for final analysis [33].

4.1.3. Micromegas

A binary file for each run, of each type, is created in CASTOR and is filled with acquired data during a run. Two types of signal are created. A micromesh pulse is created when drifted electrons hit the micromesh. Other signal, due to an electron cluster formed in the amplification gap, is created in the X-Y strips of the anode plane. Using background and calibration data and the knowledge of parameters of an X-ray event, data is processed and those that pass the analysis are considered as X-ray events [34].

4.2. Data Analysis

An upper limit for the coupling constant of the axion-photon coupling is obtained by analyzing the data collected. The $g - m_a$ dependence given in equation (2.4) is assumed not to be the only true model. The data analysis is based on the dependence of the axion flux and of the probability of conversion of axions into photons along the magnet through the following equation which gives the event number s to be observed in a time interval δt on a detector of area A and efficiency ε

$$s = A\,\Delta t \int_0^\infty \frac{d\Phi_a}{dE_a} P_{\gamma\to a}\,\varepsilon\,dE_a \tag{4.1}$$

If we distribute s in energy bins, we get s_i, number of events in each bin, given by

$$s_i = A\,\Delta t \int_{E_o}^{E_f} \frac{d\Phi_a}{dE_a} P_{\gamma\to a}\,\varepsilon\,dE_a, \tag{4.2}$$

where the integral is taken in the limit of the energy bin. Due to the low count statistics of the CAST experiment, Poissonian distribution is used to obtain the probability of observing an event count n_i in an energy bin i [8].

$$P(n_i, \mu_i) = e^{-\mu_i} \frac{\mu_i^{n_i}}{n_i!}, \tag{4.3}$$

where μ_i is the expected number of events in a bin i, which is sum of the expected axion count and the estimated background count, $\mu_i = s_i + b_i$. The background b_i is estimated from the data collected during non-tracking periods. A joint probability of observing n_i in each bin i is obtained by the multiplication of each probability given by equation (4.3).

$$P(\{n_i\}, \{\mu_i\}) = \prod_{i=1}^{N} P(n_i, \mu_i) = \prod_{i=1}^{N} e^{-\mu_i} \frac{\mu_i^{n_i}}{n_i!}, \tag{4.4}$$

where N is the number of bins. The best fit to this joint probability distribution is obtained by maximizing the likelihood function L defined by

$$L = \frac{\prod_{i=1}^{N} e^{-\mu_i} \frac{\mu_i^{n_i}}{n_i!}}{\prod_{i=1}^{N} e^{-n_i} \frac{n_i^{n_i}}{n_i!}}. \tag{4.5}$$

Investigating equations (2.36), (2.37) and (2.38), we realize that equation (4.1) is proportional to g^4, which is the only unknown parameter in the experiment. Therefore, maximizing the likelihood function results in an estimation of the axion-photon coupling.

We may also want to maximize $\ln(L)$ since it is an easier function to work with. Conveniently, we define

$$S \equiv -2 \ln(L) \tag{4.6}$$

that should be minimized due to the minus sign. Then, a further computational sim-

plification arises due to the fact that S converges to a χ^2 distribution (Appendix C) if the number of bin N is high enough [12].

After having obtained the best fit value of g^4, we need to determine the confidence interval of this value. Bayesian probability approach is used to determine 95% confidence interval of g^4. For a given dataset $\{n_i\}$, the bayesian probability is given as

$$P(g^4|\{n_i\}) = \frac{P(\{n_i\}|g^4)P(g^4)}{P(\{n_i\})}, \tag{4.7}$$

where $P(\{n_i\}|g^4)$ is the likelihood function L, $P(g^4)$ is the prior probability density function and $P(\{n_i\})$ is the probability to observed dataset $\{n_i\}$. The prior probability density function encodes the hypothetical probability that a value of g^4 is observed without any knowledge of data. In the CAST experiment, this term is a unit step function, meaning that 1 if g^4 is not negative. Therefore, we get

$$P(g^4|\{n_i\}) = \frac{e^{-\chi^2/2}}{\int_0^\infty e^{-\chi^2/2}\, d(g^4)}, \qquad g^4 \geq 0 \tag{4.8}$$

To get a confidence interval of 95%, we integrate $P(g^4|\{n_i\})$ with respect to $d(g^4)$ and equate it to 0.95 with the upper limit of the integral to be determined.

$$0.95 = \int_0^{(g^4)_{up}} P(g^4|\{n_i\})\, d(g^4). \tag{4.9}$$

The upper limit of this integral is the fourth power of the value of the axion-photon coupling constant below the fourth root of which the actual value of the axion-photon coupling constant resides.

Since there are three detectors in the CAST experiment, three different axion-photon coupling limits are obtained by analyzing seperate datasets from these detectors. An overall limit on the axion-photon coupling constant is obtained by multiplying the Bayesian probability of datasets from each detectors and determining the upper limit of the $d(g^4)$ integral of the combined Bayesian probability so that the integration

yields 0.95 [8].

$$P_{all}(g^4|\{m_i\}) = \prod_{d=1}^{3} P_d(g^4|\{n_i\}_d), \tag{4.10}$$

where d stands for detector type and $\{m_i\}$ is the combined dataset.

$$0.95 = \int_0^{(g^4)^{all}_{up}} P_{all}(g^4|\{m_i\}). \tag{4.11}$$

The χ^2 minimization of the collected data collected during Phase I of the CAST experiment resulted in a g^4 upper limit of 8.8×10^{-11} GeV^{-1}. In case of Phase II, an upper limit of g^4 is obtained for every pressure setting which corresponds to a specific axion mass. An overall upper limit of 2.17×10^{-10} on g^4 was obtained by the

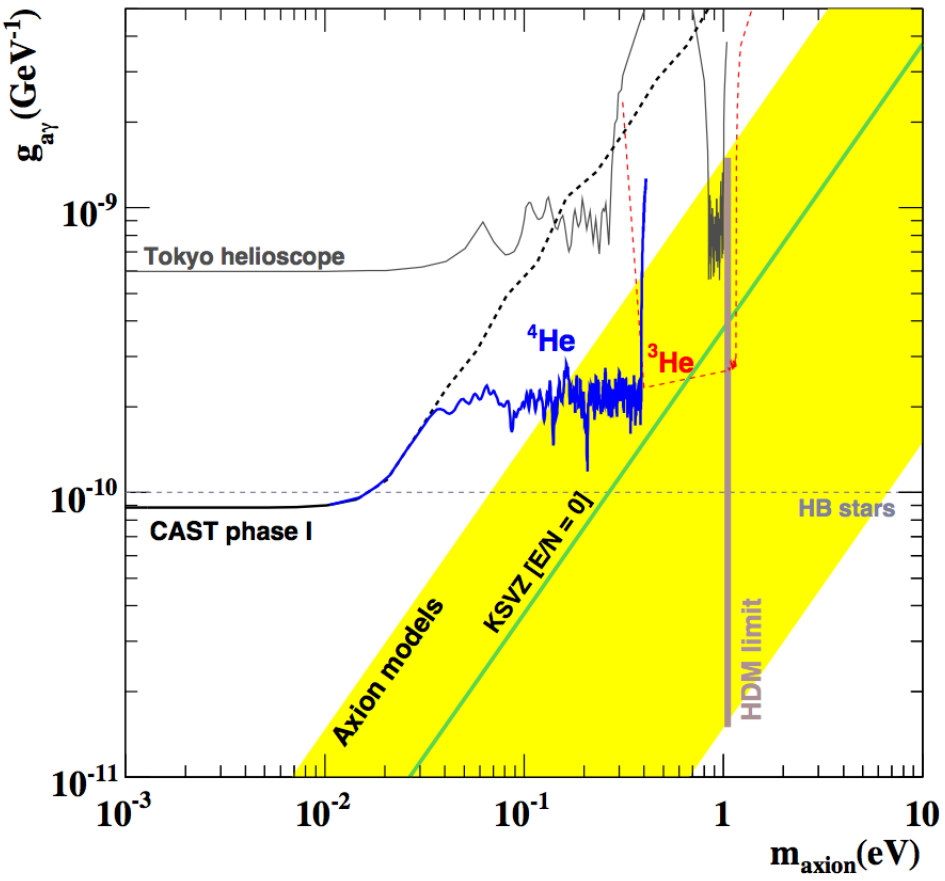

Figure 4.1. The exclusion plot obtained after Phase II with ^{4}He [8]

use of equation (4.9), where in this case the Bayesian probability is the multiplication of Bayesian probabilities of each dataset collected by different detectors at different pressure steps (Figure 4.1) [8].

4.3. Phase II ^{4}He Data Survey

The fact that any axions could not be observed until now and that the data analysis procedure is very delicate due to low statistics makes arise the necessity of reconsidering events recorded during the whole experiment. Therefore, events from each phase of the experiment collected by each detector should be gathered together and presented in a structured form to investigate possible evolutionary patterns of parameters of the events and of the experimental setup and possible correlations between these parameters, most important of which are event energy, event timestamp, event position within detector, magnet position, pressure setting and magnetic field value of the magnet, the last three of which recorded at event time.

As a first step towards the aforementioned investigations, a preliminary survey was done on the data of Phase II with ^{4}He. Tracking and background count rates of each detector versus pressure settings were plotted to have a general picture of the results obtained in Phase II with ^{4}He (Figures 4.2 and 4.4). Spectra of TPC and MicroMEGAS events at the 4.000303 mbar pressure setting were plotted as examples; the CCD count rate which is zero or very close to zero makes such a plot uninteresting (Figures 4.3 and 4.7). Finally, the event positions within the MicroMEGAS detector are plotted (Figure 4.8).

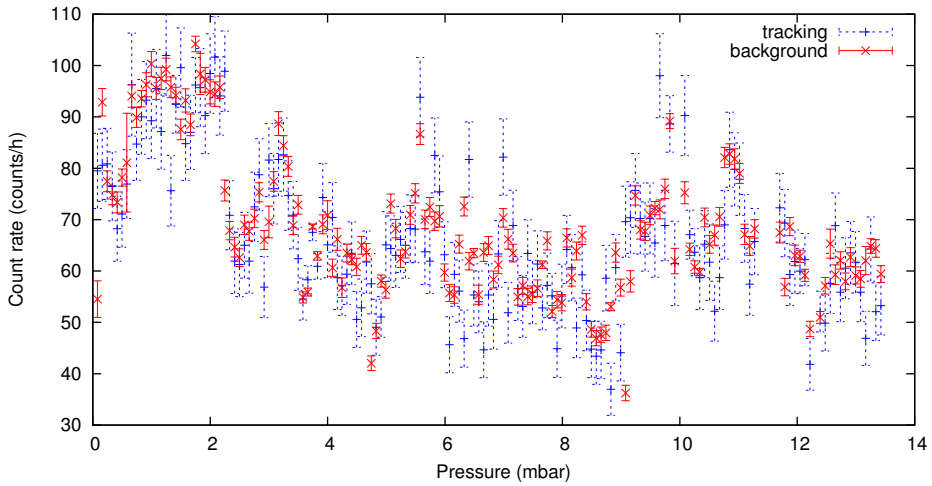

Figure 4.2. TPC count rate vs. pressure

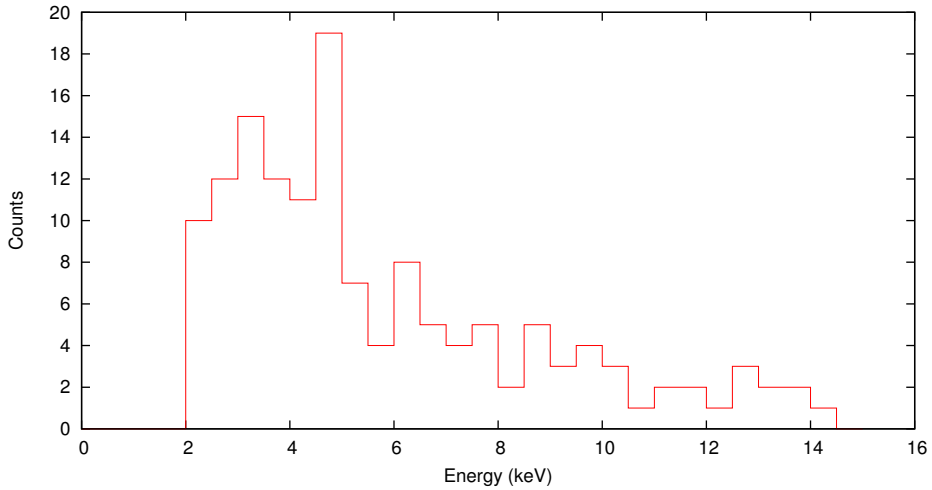

Figure 4.3. Spectrum of TPC tracking events at the 4.000303 mbar pressure setting

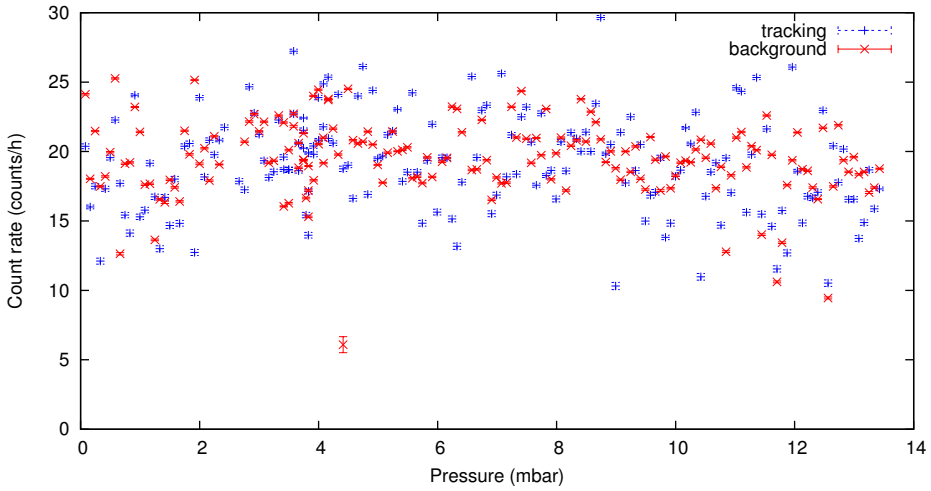

Figure 4.4. MicroMEGAS count rate vs. pressure

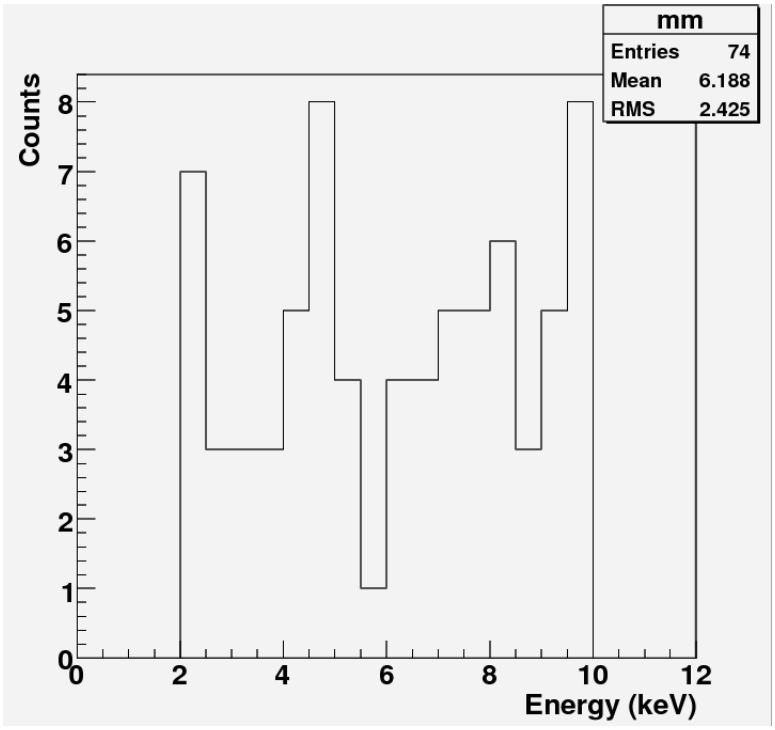

Figure 4.5. Spectrum of MicroMEGAS tracking events at the 4.000303 mbar pressure setting

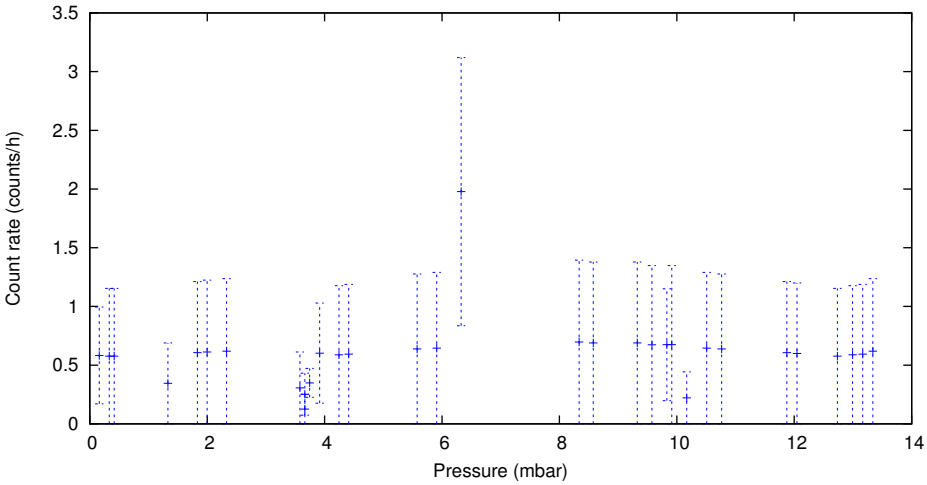

Figure 4.6. CCD tracking count rate vs. pressure

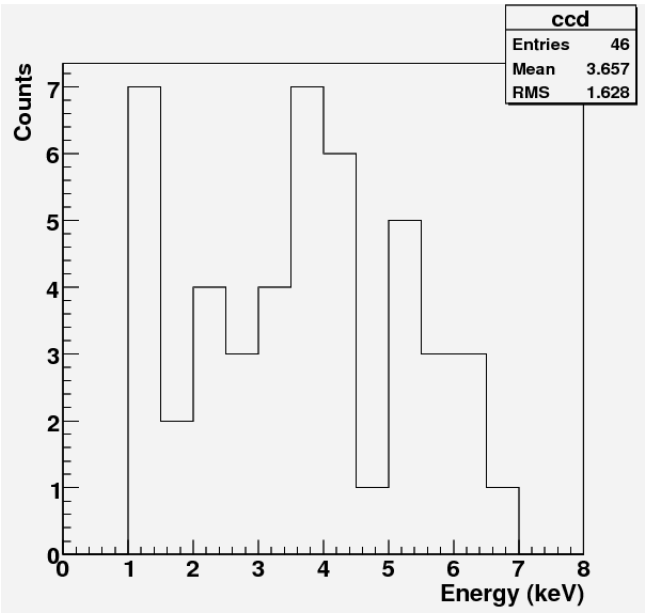

Figure 4.7. Spectrum of CCD tracking events at all pressure settings

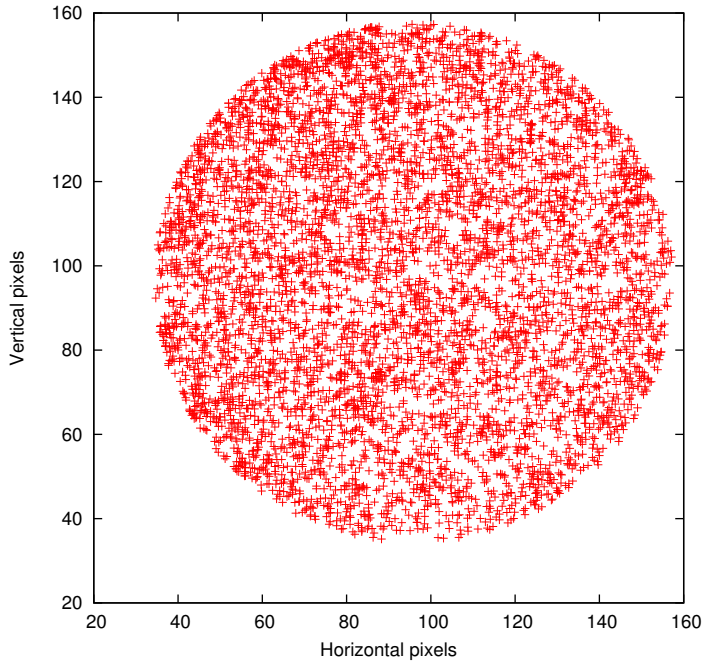

Figure 4.8. Positions of MicroMEGAS tracking events

5. CONCLUSIONS

Every aspect of the CAST experiment, namely the theory of solar axion production, the principle of solar axion detection, necessary technologies to build CAST, the data acquisition during the experiment, the theory of data analysis and the application of this last theory to the analysis of CAST data, were reviewed. Additionally, a survey of data collected during the first part of the second phase of the experiment was done.

Two different axion production mechanisms in the Sun were shown to be equivalent if the energy of the incoming photon, or the transverse electromangetic wave, is smaller than the Debye-Hückel wavenumber (with c=$\hbar$=k_B=1). Conveniently, an extensive review on electromagnetic plasma excitations was done as well.

It is also shown how the calculation of the solar axion flux using the actual solar model and the total decay rate of a photon into an axion, combined with detection principle that CAST is based on provides the specifications of necessary technologies to build the CAST experiment.

Besides theoretical subjects, technical aspects of CAST were mentioned, without going into details of many complications stemming from every component of it. Data acquisition and analysis methods were also investigated.

In order to provide a general picture of data collected when the cold bores of the magnet were filled with ^{4}He as a buffer gas, several plots were drawn and presented and event rates were listed.

APPENDIX A: Debye-Hückel Screening

In a plasma, each charged particle creates around itself a cloud of charged particles. An electrostatic potential Φ is created by this accumulation of charges. Each charged particle in this electric field has a potential energy of $Z_i e\Phi$. Then, the Boltzmann distribution n_i describing the spatial density of these particles of kind i is given by

$$n_i(\mathbf{r}) = n_{i0} e^{-(Z_i e\Phi/T)}, \tag{A.1}$$

where n_{i0} is the mean density and T is the plasma temperature [16].

The electrostatic Poisson's equation is

$$\nabla^2\Phi = -\rho, \tag{A.2}$$

where ρ is charge density and Φ is electrostatic potential. Substituting equation (A.1) in equation (A.2), we get

$$\nabla^2\Phi = -e\sum_i Z_i n_i. \tag{A.3}$$

Assuming $eZ_i\Phi/T$ is small, equation (A.1) can be linearized.

$$n_i = n_{i0} - \frac{n_{i0} e Z_i}{T}\Phi. \tag{A.4}$$

Substituting this in equation (A.3) and imposing the quasineutrality condition of the plasma,

$$\sum_i Z_i n_{i0} = 0, \tag{A.5}$$

we get

$$\nabla^2\Phi - \kappa^2\Phi = 0, \tag{A.6}$$

where

$$\kappa^2 = \frac{e^2}{T}\sum_i Z_i^2 n_i \tag{A.7}$$

is the square of the *Debye-Hückel wavenumber*.

APPENDIX B: Transverse and Longitudinal Electromagnetic Plasma Excitations

For an unbounded spatially homogeneous plasma in a stationary state, the field of electrical induction is given as [15]

$$\frac{\partial \mathbf{D}}{\partial t} = \frac{\partial \mathbf{E}}{\partial t} + \mathbf{J} \tag{B.1}$$

Therefore the Maxwell's equations can be rewritten as

$$\nabla \cdot \mathbf{D} = 0 \tag{B.2}$$

$$\nabla \times \mathbf{E} = -\frac{\partial \mathbf{B}}{\partial t} \tag{B.3}$$

$$\nabla \cdot \mathbf{B} = 0 \tag{B.4}$$

$$\nabla \times \mathbf{B} = \frac{\partial \mathbf{D}}{\partial t} \tag{B.5}$$

Then the wave equation is

$$\nabla \times \nabla \times \mathbf{E} + \frac{\partial^2 \mathbf{D}}{\partial t^2} = 0 \tag{B.6}$$

If the electric field is weak enough, equation (B.1) translates into a linear connection between the induction $\mathbf{D}$ and the electric field $\mathbf{E}$ [35],

$$D_i(\mathbf{k}, \omega) = \epsilon_{ij} E_j(\mathbf{k}, \omega). \tag{B.7}$$

If we take the Fourier transform of equation (B.6), we get the macroscopic field equation in a medium without external currents.

$$\Lambda_{ij}(\mathbf{k},\omega)E_j(\mathbf{k},\omega) = 0 \tag{B.8}$$

where

$$\Lambda_{ij}(\mathbf{k},\omega) \equiv \epsilon_{ij}(\mathbf{k},\omega) - \left(\delta_{ij} - \frac{k_i k_j}{k^2}\right)\eta^2 \tag{B.9}$$

with $\eta = k/\omega$, the refraction index of the wave. Equation (B.9) has nontrivial solutions if the determinant of Λ_{ij} is zero.

$$\Lambda(\mathbf{k},\omega) \equiv ||\Lambda_{ij}(\mathbf{k},\omega)|| = 0 \tag{B.10}$$

This is the *dispersion equation* of a medium [15].

In an isotropic plasma the dielectric permittivity ϵ_{ij} is conventionally expressed as [15]

$$\epsilon_{ij}(\mathbf{k},\omega) = \epsilon_l(k,\omega)\frac{k_i k_j}{k^2} + \ \epsilon_t(k,\omega)\left(\delta_{ij} - \frac{k_i k_j}{k^2}\right), \tag{B.11}$$

where ϵ_l is the longitudinal dielectric permittivity and ϵ_t is the transverse dielectric permittivity. Therefore, the wave equation (B.8) takes the form

$$\left[\epsilon_l(k,\omega)\frac{k_i k_j}{k^2} + \ (\epsilon_t(k,\omega) - \eta^2)\left(\delta_{ij} - \frac{k_i k_j}{k^2}\right)\right]E_j(\mathbf{k},\omega) = 0, \tag{B.12}$$

and the determinant of the tensor Λ_{ij} becomes

$$\Lambda(\mathbf{k},\omega) \equiv \epsilon_l(\mathbf{k},\omega)[\epsilon_t(\mathbf{k},\omega) - \eta^2]^2 = 0, \tag{B.13}$$

giving rise to two dispersion equations. The dispersion equation for longitudinal waves in a spatially homogeneous, isotropic medium is

$$\epsilon_l(\mathbf{k},\omega) = 0, \tag{B.14}$$

and the dispersion equation for transverse waves in such a medium is

$$\epsilon_t(\mathbf{k},\omega) - \eta^2 = 0. \tag{B.15}$$

If the plasma is assumed collisionless and in thermal equilibrium with Maxwellian velocity distribution which is

$$f_i(v) = n_i\left(\frac{m_i}{2\pi T_i}\right)^{3/2} exp(-\frac{m_i v^2}{2T_i}), \tag{B.16}$$

using Vlasov's equations

$$\frac{\partial f_i}{\partial t} + \mathbf{v_i}\cdot\frac{\partial f_i}{\partial \mathbf{r}} + \frac{Z_i e}{m_i}\left(\mathbf{E} + \ \mathbf{v_i}\times\mathbf{B}\right)\frac{\partial f_i}{\partial \mathbf{v_i}} = 0, \tag{B.17}$$

where m_i is the mass and $\mathbf{v}_i$ the fluid velocity of the plasma component i, the dielectric permittivities are found as [15]

$$\epsilon_l(k,\omega) = 1 + \sum_i \frac{\kappa_i^2}{k^2}[1 - \phi(z_i) + \ i\sqrt{\pi}z_i e^{-z_i^2}] \tag{B.18}$$

and

$$\epsilon_t(k,\omega) = 1 - \sum_i \frac{\omega_{pi}^2}{\omega^2}[\phi(z_i) - \ i\sqrt{\pi}z_i e^{-z_i^2}], \tag{B.19}$$

where the contribution of plasma component i to the square of the Debye-Hückel wavenumber κ^2 is

$$\kappa_i^2 = \frac{Z_i^2 e^2 n_i}{T_i}, \tag{B.20}$$

the plasma frequency of the plasma component i is

$$\omega_{pi} = \sqrt{\frac{Z_i^2 e^2 n_i}{m_i}}, \tag{B.21}$$

the variables z_i is

$$z_i = \sqrt{\frac{3}{2}} \frac{\omega}{k s_i}, \tag{B.22}$$

the variable s_i is

$$s_i = \sqrt{\frac{3T_i}{m_i}}, \tag{B.23}$$

and finally the function $\phi(z_i)$ is

$$\phi(z_i) = 2z_i \, e^{-z_i^2} \int_0^{z_i} dx \, e^{x^2}. \tag{B.24}$$

In case of $z \gg 1$, which is the high frequency limit, the asymptotic expansion of $\phi(z)$ is [15]

$$\phi(z) = e^{-z^2} \left[e^{z^2} \left(1 + \frac{1}{2z^2} + \frac{3}{4z^4} \right) - i\sqrt{\pi} z \right]. \tag{B.25}$$

Therefore, putting $\phi(z)$ into equation (B.18) and equating this equation to zero, we get the dispersion relation of a longitudinal wave in a spatially homogeneous and isotropic two-component (purely hydrogen) plasma in the high frequency limit as

$$\omega^2 = \omega_p^2 \left(1 + \frac{3T}{m} k^2 \right), \tag{B.26}$$

where the temperature of the components are assumed to be equal, $T = T_e = T_p$. Therefore, with the fact that proton is much heavier than electron, the $1/z$ terms coming from the protons in the asymptotic expansion of $\phi(z_i)$ is neglected. Moreover, due

to the mass difference between proton and electron implies that the plasma frequency of electron is much higher than the plasma frequency of protons (hydrogen nuclei), $\omega_p = \omega_{pe} \gg \omega_{pp}$. Therefore, neglect of the $1/z_p$ terms can be interpreted as the neglect of the ion plasma frequency since it turns out that $\omega_i^2 = \kappa_i^2(T_i/m_i)$ when equations $B.20$-$B.23$ are investigated. Notice that in the nonrelativistic limit, $\omega = \omega_p$, but when the second term is comparable to the first term, ω diverges from ω_p for different k's. This divergence is possible when $k^2 \gtrsim m_e/3T = \kappa_e^2$ and is called the *Landau damping*.

In a similar manner, putting $\phi(z)$ into equation (B.19) and using the dispersion equation B.15, we get the dispersion relation in the high frequency limit for a transverse electromagnetic field in a plasma with aforementioned characterictics,

$$\omega^2 = \omega_p^2 + \left(1 + \frac{T\omega_p}{m_e\omega^2}\right)k^2, \tag{B.27}$$

where the ion plasma frequency is again neglected.

APPENDIX C: χ^2 distribution

If measurements of events on a detector are Gaussian distributed, their likelihood function is

$$L = \prod_{i=1}^{N} \frac{1}{\sigma_i \sqrt{2\pi}} \exp\left(\frac{-(n_i - \mu_i)^2)}{2\sigma_i^2}\right), \tag{C.1}$$

which can be rewritten as

$$L = \prod_{i=0}^{N} \frac{1}{\sigma_i \sqrt{2\pi}} \exp\left(-\frac{1}{2} \sum_{i=0}^{N} \frac{(n_i - \mu_i)^2}{\sigma_i}\right) \tag{C.2}$$

To maximize L, we need to minimize the summation which is defined as χ^2.

$$\chi^2 \equiv \sum_{i=0}^{N} \frac{(n_i - \mu_i)^2}{\sigma_i^2} = -2 \ln(L) + \text{constant}. \tag{C.3}$$

APPENDIX D: Phase II ^{4}He Event Rates

Table D.1. Event rates at each pressure setting of Phase II with ^{4}He. CCD background event rate is taken to be 0.096753 counts/h for all pressure settings.

Pressure (mbar)	MicroMEGAS		TPC		CCD
	Tracking event rate (counts/h)	Background event rate (counts/h)	Tracking event rate (counts/h)	Background event rate (counts/h)	Tracking event rate (counts/h)
0.079900	20.3768	24.1277	79.4913	54.5313	
0.161620	16.0066	18.0327	80.5969	92.8681	0.582477
0.244470	17.4932	21.476	80.8455	77.4858	
0.331380	12.106	17.4873	76.4706	74.7866	0.576784
0.415160	17.3115	18.2033	68.2353	73.3617	0.576784
0.496980	19.5609	19.9573	71.0836	78.2102	
0.579850	22.2697	25.2642	76.9428	81.0913	
0.662710	17.7085	12.6349	96.279	94.0692	
0.745520	15.4223	19.1174	84.7059	89.9142	
0.828410	14.1219	19.2133	90	93.5569	
0.911760	24.0517	23.2061	93.2706	96.2741	
0.996340	15.2961	21.4171	89.2661	100.32	
1.080930	15.7817	17.6079	95.5104	95.5386	
1.165590	19.1564	17.6752	87.1565	97.4888	
1.248810	16.7403	13.6338	101.992	99.2371	
1.332060	12.9989	16.5536	75.625	95.7692	0.344761

Pressure (mbar)	MicroMEGAS		TPC		CCD
	Tracking event rate (counts/h)	Background event rate (counts/h)	Tracking event rate (counts/h)	Background event rate (counts/h)	Tracking event rate (counts/h)
1.415320	16.6969	16.3403	92.4658	94.2006	
1.498770	14.6688	17.9623	99.5998	87.5632	
1.581888	18.0148	17.4163	84.7914	93.2043	
1.665199	14.8293	16.4057	86.9998	88.4512	
1.748413	20.3767	21.4962	96.213	104.207	
1.831620	20.578	19.7982	95.6932	98.3759	0.605906
1.915167	12.7303	25.1531	90.2423	97.2232	
1.998118	23.8794	19.1195	98.4372	94.8718	0.612194
2.081380	18.1732	20.2341	101.633	94.4453	
2.164650	20.8137	17.9075	94.085	95.7765	
2.247905	19.7711	21.0938	98.901	75.6784	
2.331150	20.8235	19.0689	70.8509	67.865	0.618399
2.416738	61.9148	64.6539			
2.49940	61.2765	62.5958			
2.58221	65.0072	68.9968			
2.664827	61.9383	67.7579			
2.755600	17.2463	20.7066	72.5	70.2472	
2.835362	24.6637	22.1578	78.75	75.3381	
2.917715	22.7721	22.6925	56.875	66.0478	
3.000066	21.2439	21.457	81.5933	69.5679	
3.082414	19.3428	22.1488	76.0301	77.4402	
3.164798	18.126	19.1826	81.7054	88.6971	
3.247668	18.5397	19.3343	82.6532	84.395	
3.330617	22.2652	22.5935	74.694	80.3458	
3.413622	19.5957	22.0873	70.8614	68.8917	

Pressure (mbar)	MicroMEGAS		TPC		CCD
	Tracking event rate (counts/h)	Background event rate (counts/h)	Tracking event rate (counts/h)	Background event rate (counts/h)	Tracking event rate (counts/h)
3.414000	18.7035	16.047			
3.496677	18.6877	16.2768	62.3823	72.8874	
3.496997	18.6837	20.1036			
3.579783	22.7124	21.8146	54.5549	54.8593	
3.580044	27.224	22.7218	0.306084		
3.662917	18.6195	18.8319	58.2922	55.9131	0.378888
3.663103	20.6014	20.6095	0.252592		
3.746065	21.532	19.3753	67.5397	68.6548	
3.746155	20.2391	21.3191			0.348856
3.746700	22.4125	19.4052			
3.788300	15.4253	16.6513			
3.827981	13.9737	17.1938			
3.829278	19.9002	18.9585	60.9144	62.9445	
3.830000	17.1338	15.2933			
3.912370	20.4006	24.0003	74.3066	69.0945	0.60241
3.917193	19.8011	17.9295			
3.995488	23.8871	24.4517			
4.000303	20.8205	20.5301	65.0984	70.8697	
4.078612	21.7816	20.9886			
4.083391	24.8685	19.1684	70.4349	60.6408	
4.161740	25.3554	23.7087			
4.166495	20.9489	23.7915	58.6958	66.1725	
4.244866	20.6051	21.6419	57.1242	56.7446	0.588187
4.328010	24.1113	19.7804	59.379	63.5127	
4.411169	18.7553	6.08712	63.4466	62.2117	0.594011

Pressure (mbar)	MicroMEGAS		TPC		CCD
	Tracking event rate (counts/h)	Background event rate (counts/h)	Tracking event rate (counts/h)	Background event rate (counts/h)	Tracking event rate (counts/h)
4.494329	19.0149	24.5148	50.5882	60.8094	
4.577502	16.6184	20.8219	52.8366	65.0178	
4.660667	23.9989	20.5812	61.7416	63.6206	
4.743827	26.1206	20.7076	57.5233	42.0539	
4.826962	16.9108	21.4345	49.0579	48.333	
4.910105	24.405	20.5063	51.0595	58.0446	
4.993230	19.4881	19.0382	65.1062	56.326	
5.076368	19.6739	17.7545	64.375	73.1238	
5.159484	21.2015	19.9188	63.0494	68.273	
5.242611	21.4703	21.4454	66.1582	62.406	
5.325727	23.04	20.0135	65.0072	63.7527	
5.408845	17.8495	20.1161	68.2585	70.9217	
5.491971	18.5139	20.301	68.1629	75.1329	
5.575286	24.2322	18.0862	93.8296	86.6662	0.63813
5.658608	18.5139	18.1774	63.7393	70.0623	
5.741942	14.8337	17.7306	61.9148	72.4719	
5.825254	19.3525	19.5783	82.5215	69.7056	
5.908559	21.9665	18.1697	75.4299	70.6598	0.645103
5.991865	15.6364	34.327	63.1691	59.703	
6.075181	19.5614	19.2596	45.6523	55.7307	
6.158526	19.552	19.538	59.348	55.334	
6.241820	15.1486	23.2337	56.0871	65.2256	
6.325309	13.1762	23.076	46.8474	72.5747	1.97784
6.408701	17.7952	21.3832	81.6983	61.9185	
6.491977			55.3333	63.491	

Pressure (mbar)	MicroMEGAS		TPC		CCD
	Tracking event rate (counts/h)	Background event rate (counts/h)	Tracking event rate (counts/h)	Background event rate (counts/h)	Tracking event rate (counts/h)
6.575263	25.398	18.6724	54	55.3857	
6.658573	19.5678	18.7144	44.6667	63.6088	
6.741845	22.9675	22.276	55.3333	64.9494	
6.825115	23.3375	19.3797	50.5918	58.3411	
6.908401	15.5167	16.5218	63.3333	61.1891	
6.991676	16.8634	18.1326	82.1859	70.3507	
7.075044	25.6149	17.7073	51.8714	66.1977	
7.158321	18.1757	17.7631	68.8635	63.4958	
7.241596	21.1906	23.2179	56.5908	54.9662	
7.324862	18.3672	21.01	53.1013	57.1131	
7.408134	22.5012	24.356	63.4089	55.0225	
7.491399	23.1982	20.9213	55.909	55.4866	
7.574669	20.6721	19.1823	61.3635	56.6434	
7.657911	17.574	20.971	52.82	61.2153	
7.741190	22.7489	19.735	57.1976	65.865	
7.824478	18.2704	23.0682	55.1724	52.1148	
7.907757	18.6405	17.9955	44.8619	54.4229	
7.991029	16.5803	19.871	55.1164	53.8309	
8.074307	20.6932	21.0054	64.1871	66.4474	
8.157585	18.6031	17.1917	60.6432	58.7121	
8.240871	21.3631	20.416	48.9281	63.896	
8.336100	20.9284	20.8107	59.265	66.9591	0.697472
8.409204	20.0104	23.7712	50.3834	54.0093	
8.492300	21.393	20.7181	44.7933	48.6435	
8.575752	20.0058	22.8695	43.415	46.9242	0.689589

Pressure (mbar)	MicroMEGAS		TPC		CCD
	Tracking event rate (counts/h)	Background event rate (counts/h)	Tracking event rate (counts/h)	Background event rate (counts/h)	Tracking event rate (counts/h)
8.659009	23.4507	22.1111	44.6513	47.6061	
8.742125	29.6499	20.8795	58.6048	47.9744	
8.825524	19.8318	19.2412	36.9768	53.0515	
8.908790	20.5003	20.0126	60.6432	63.5847	
8.992038	10.3165	18.7974	44.1042	56.776	
9.075304	21.3787	17.9666	69.6019	36.2503	
9.158568	17.7329	20.0045	70.3987	57.9854	
9.241845	22.4984	18.535	75.6816	74.7003	
9.325148	18.6263	20.3659	70.2271	68.0057	0.689589
9.408435	20.5051	18.0385	66.717	67.7174	
9.491636	14.9948	17.2644	70.2271	70.8338	
9.576031	16.8504	21.045	65.4544	72.2512	0.673968
9.660469	17.064	19.4073	98.0332	71.9924	
9.744985	19.5452	17.1872	68.8635	76.0022	
9.829533	13.8163	19.6408	88.6365	89.1721	0.674095
9.914526	14.8354	17.3522	61.4634	61.9318	0.674095
9.998774	18.2046	18.2585			
10.083500	18.6622	19.1978	90.2697	75.231	
10.168260	21.7005	19.3399	67.0786	64.2337	0.221368
10.253050	20.5518	19.23	63.6667	60.7756	
10.337990	22.8249	20.1482	58.6958	59.788	
10.422810	10.9755	20.8465	65.2175	70.4299	
10.507760	16.7747	19.5472	61.7295	65.2031	0.645103
10.592770	18.5235	20.567	52.174	67.0019	
10.677810	19.1828	17.3572	58.6958	70.5511	

Pressure (mbar)	MicroMEGAS		TPC		CCD
	Tracking event rate (counts/h)	Background event rate (counts/h)	Tracking event rate (counts/h)	Background event rate (counts/h)	Tracking event rate (counts/h)
10.763050	14.689	18.901	68.9829	82.0986	0.638239
10.848260	19.5305	12.7848	83.6168	82.7885	
10.933500	17.0322	18.2868	79.7871	81.8008	
11.018780	24.5917	21.0057	77.8722	79.0071	
11.104110	24.3324	21.4064	68.2977	67.1228	
11.189470	15.6234	18.8627	57.4467	64.8977	
11.274880	19.7758	20.3918	65.7304	68.2075	
11.360360	25.3313	20.0975			
11.445880	15.4892	14.0068			
11.531420	21.6302	22.5929			
11.616990	14.6057	19.7619			
11.702660	11.5471	10.6075	72.3213	67.4905	
11.788360	15.7457	13.4331	69.3258	56.8912	
11.874130	12.698	17.5791	59.3069	68.6464	0.605906
11.959920	26.0848	19.3669	61.8369	63.043	
12.045770	18.5862	21.3729	59.9786	62.8612	0.599948
12.131670	14.8538	18.7238	62.212	59.1701	
12.217610	16.7774	18.6123	41.8463	48.7203	
12.303610	16.6556	17.4023			
12.389690	17.0626	16.569	52.1212	50.962	
12.475740	22.961	21.7042	49.8682	57.1371	
12.561850	10.5238	9.45316	57.5859	65.3364	
12.648010	20.408	17.4855	68.8235	59.2864	
12.734220	17.7731	21.8974	55.8824	62.0612	0.576784
12.820470	20.1786	19.376	60.5433	57.986	

Pressure (mbar)	MicroMEGAS		TPC		CCD
	Tracking event rate (counts/h)	Background event rate (counts/h)	Tracking event rate (counts/h)	Background event rate (counts/h)	Tracking event rate (counts/h)
12.906770	16.5561	18.5317	63.5294	62.7027	
12.993110	16.563	19.5978	61.7076	59.1334	0.588235
13.079500	13.7396	18.3566	55.8824	58.4795	
13.165900	14.8803	18.5332	46.8999	62.0396	0.594061
13.252400	18.6809	17.0478	64.2857	64.8626	
13.339000	15.8765	17.4055	52.0862	64.3833	0.618555
13.425600	17.3065	18.7634	53.2654	59.4039	

REFERENCES

1. Peccei, R. D. and H. R. Quinn, "CP Conservation in the Presence of Pseudoparticles", *Phys. Rev. Lett.*, Vol. 38, No. 25, pp. 1440-1443, June 1977.

2. Weinberg, S., "A New Light Boson?", *Phys. Rev. Lett.*, Vol. 40, No. 4, pp. 223-226, January 1978.

3. Wilczek, F., "Problem of P and T Invariance in the Presence of Instantons", *Phys. Rev. Lett.*, Vol. 40, No. 5, pp. 279-282, January 1978.

4. Raffelt, G. G., "Astrophysical Axion Bounds Diminished by Screening Effects", *Phys. Rev. D*, Vol. 33, No. 4, pp. 897-909, February 1986.

5. Raffelt, G. G., "Plasmon Decay into Low-Mass Bosons in Stars", *Phys. Rev. D*, Vol. 37, No. 6, pp. 1356-1359, March 1988.

6. Sikivie, P., "Experimental Tests of the "Invisible" Axion", *Phys. Rev. Lett.*, Vol. 51, No. 16, pp. 1415-1417, October 1983.

7. Andriamonje, S. et al., "An Improved Limit on the Axion-Photon Coupling from the CAST Experiment", *JCAP*, April 2007.

8. Andriamonje, S. et al., "Probing eV-Scale Axions with CAST", *JCAP*, February 2009.

9. Dicus, D. A. et al., "Astrophysical Bounds on the Masses of Axions and Higgs Particles", *Phys. Rev. D*, Vol. 18, No. 6, pp. 1829-1834, September 1978.

10. Primakoff, H., "Photo-Production of Neutral Mesons in Nuclear Electric Fields and the Mean Life of the Neutral Meson", *Phys. Rev.*, Vol. 81, No. 5, p. 899, January 1951.

11. Fukugita, M., S. Watamura and M. Yoshimura, "Light Pseudoscalar Particle and Stellar Energy Loss", *Phys. Rev. Lett.*, Vol. 48, No. 22, pp. 1522-1525, May 1982.

12. Amsler, C. et al., "The Review of Particle Physics" *Phys. Lett. B*, Vol. 667, No. 1-5, July 2008.

13. Raffelt, G. and L. Stodolsky, "Mixing of the Photon with Low-Mass Particles", *Phys. Rev. D*, Vol. 37, No. 5, pp. 1237-1249, March 1998.

14. Raffelt, G., *Stars as Laboratories for Fundamental Physics*, University of Chicago Press, Chicago, 1996.

15. Sitenko, A. and V. Malnev, *Plasma Physics Theory*, Chapman and Hall, London, 1995.

16. Landau, L. D. and E. M. Lifshitz, *Statistical Physics: Course of Theoretical Physics, Vol. 5*, Pergamon, 1980

17. Serpico, P. D. and G. G. Raffelt, "New Calculation of Solar Axion Flux", *Internal CAST Report*, January 2005.

18. Bahcall, J. N. and M. H. Pinsonneault, "What do we (not) know theoretically about solar neutrino fluxes?" *Phys. Rev. Lett.*, Vol. 92, No. 12, p. 121301, March 2004

19. van Bibber, K. et al., "Design for a Practical Laboratory Detector for Solar Axions", *Phys. Rev. D*, Vol. 39, No. 8, pp. 2089-2099, April 1989.

20. Lazarus, D. M. et al., "Search for Solar Axions", *Phys. Rev. Lett.*, Vol. 69, No. 16, pp. 2333-2336, October 1992.

21. Kang, D., *Search for Solar Axions with the CCD detector at CAST (CERN Axion Solar Telescope)*, Ph.D. Thesis, Albert-Ludwigs-Universität Freiburg, January 2007

22. Zioutas, K. et al., "A Decommissioned LHC Model Magnet as an Axion Telescope", *Nucl. Instrum. Meth. Phys. Res.*, Sect. A, Vol. 425, No. 3, pp. 480-489, January 1999.

23. Barth, K. et al., "Cryogenics for the CERN Solar Axion Telescope (CAST) Using a LHC Dipole Prototype Magnet", November 2002. *CERN Divisional Report*

24. Armendariz, J. R., *Search for Solar Axions with the Time Projection Chamber of the CERN Axion Solar Telescope with 4-Helium as Buffer Gas* Ph.D. Thesis, Universidad de Zaragoza, September 2008

25. Zioutas, K. et al., "First Results from the CERN Axion Solar Telescope", *Phys. Rev. Lett.*, Vol. 94, No. 12, p. 121301, April 2005.

26. Autiero, D. et al., "The CAST Time Projection Chamber", *New J. Phys.*, Vol. 9, No. 6, p. 171, June 2007

27. Berkol, O. D., *Searching for Solar Axions in CAST-CERN Axion Solar Telescope* M.S. Thesis, Boğaziį Üniversitesi, April 2006

28. Kuster, M. et al., "The X-Ray Telescope of CAST" *New J. Phys.*, Vol. 9, No. 6, p.169, June 2007

29. Vogel, J. K., *Searching for Solar Axions in the eV-Mass Region with the CCD Detector at CAST* Ph.D. Thesis, Albert-Ludwigs-Universität Freiburg, April 2009

30. Nordt, A., *Suche nach Solaren Axionen mit dem Röntgenteleskop des CAST experiments (Phase II)* Ph.D. Thesis, Technischen Universität Darmstadt, November 2008

31. Abbon, P. et al., "The Micromegas detector of the CAST experiment", *New J. Phys.*, Vol. 9, No. 6, p.170, June 2007

32. "Micromegas Detectors", *Internal CAST poster*, June 2008

33. Lizarraga, B. B., *A TPC for Solar Axion Searches in the CAST experiment at CAST* Ph.D. Thesis, Universidad de Zaragoza, April 2006

34. Dafni, T., *A Search for Solar Axions with the MICROMEGAS Detector in CAST* Ph.D. Thesis, Technischen Universität Darmstadt, June 2005

35. Kirzhnits, D. A., "General Properties of Electromagnetic Response Functions", *Usp. Fiz. Nauk*, Vol. 152, pp. 399-422, July 1987.